Band structure, evanescent states, and transport in spin tunnel junctions

2003 J. Phys.: Condens. Matter 15 R1603

(http://iopscience.iop.org/0953-8984/15/41/R01)

INSTITUTE OF PHYSICS PUBLISHING JOURNAL OF PHYSICS: CONDENSED MATTER

J. Phys.: Condens. Matter **15** (2003) R1603–R1639 PII: S0953-8984(03)21199-1

TOPICAL REVIEW

Band structure, evanescent states, and transport in spin tunnel junctions

X-G Zhang[1] **and W H Butler**[2,3]

[1] Computational Science and Mathematics Division, Oak Ridge National Laboratory, PO Box 2008, Oak Ridge, TN 37831-6114, USA
[2] Center for Materials for Information Technology and Department of Physics, University of Alabama, Tuscaloosa, AL 35487-0209, USA
[3] Metals and Ceramics Division, Oak Ridge National Laboratory, PO Box 2008, Oak Ridge, TN 37831-6114, USA

Received 8 July 2003
Published 3 October 2003
Online at stacks.iop.org/JPhysCM/15/R1603

Abstract

First-principles based electronic structure calculations provide important insight into spin-dependent transport in tunnelling junctions with magnetic electrodes. They have shown that Bloch electrons are qualitatively different from free electrons in determining the tunnelling probability and magnetoresistance of tunnelling junctions, and that tunnelling wavefunctions within the barrier region are usually different from those modelled by a simple barrier potential. Several factors are important in determining the tunnelling current and magnetoresistance of a tunnelling junction. These include the symmetry of the Bloch wavefunctions, the presence or absence of interface resonance states, the nature of the chemical bond between the electrode atoms and the atoms in the barrier layer, and the complex bands (evanescent states) within the barrier layer.

(Some figures in this article are in colour only in the electronic version)

Contents

1. Introduction

It has long been known that the electronic structure of materials really consists of two electronic structures, corresponding to the two different spin states of the electrons. In most materials, i.e. those that are not magnetic, these electronic structures are equivalent. In these materials, the effect of the two 'parallel' electronic structures is trivial; materials properties such as specific heat or electrical conductivity are simply multiplied by a factor of two. In magnetic materials, the electronic structures corresponding to the two spin states will be different so that one may imagine two different materials coexisting in the same object. This picture is most appropriate when the effects of spin–orbit coupling can be neglected and the magnetic moments in the material are collinear.

Until relatively recently, it has been difficult to observe these two different electronic structures. The discovery of the giant-magnetoresistance (GMR) effect [1] in 1988 and its rapid development and application dramatically changed this situation. The GMR effect is observed experimentally as a change in the electrical resistivity of a magnetically inhomogeneous metallic material that occurs when an applied magnetic field aligns the magnetic moments in different regions. The discovery of GMR focused the attention of the scientific community on the importance of the spin degree of freedom in electron transport problems which in turn led to the discovery or rediscovery of other spin related transport phenomena. One of these phenomena is the so-called 'colossal magnetoresistance' [2], a large change in resistance with magnetic field that can occur in certain oxide materials such as $La_{0.67}A_{0.33}MnO_3$ where A represents an alkaline earth element. The large magnetoresistance seems to be associated with a metal to insulator transition that occurs with increasing temperature and is affected by an applied magnetic field.

The phenomenon of spin-dependent tunnelling is another spin-dependent transport effect that may soon become technologically important and is the subject of this paper. Spin-dependent tunnelling, sometimes called tunnelling magnetoresistance or TMR, is the dependence of the tunnelling current between ferromagnetic electrodes separated by a nonconducting barrier on the relative orientation of the magnetic moments of the two electrodes. The first published report of spin-dependent tunnelling was by Julliere [3] in 1975 who measured the resistance of a Fe|Ge|Co sandwich at a temperature of 4.2 K. He observed a decrease in resistance of 14% when the magnetic moments in the Fe and Co electrodes were switched from antiparallel to parallel. Julliere's work may have been inspired in part by the work of Tedrow and Meservey [4] who had earlier measured the spin dependence of tunnelling currents through an amorphous aluminium oxide tunnel barrier separating various ferromagnetic electrodes from superconducting aluminium.

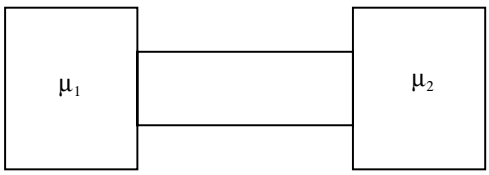

Figure 1. Two electron reservoirs connected by a sample.

Work continued on TMR in the decades following Julliere's paper [5–7] with the pace increasing after the discovery of GMR. Interest became quite intense after papers in 1995 that demonstrated changes in resistance of more than 10% at room temperature [8, 9]. TMR based devices are at present considered the most likely candidates for the next major applications of spin-dependent transport. Magnetic random access memory and logic devices based on TMR are currently under development [10, 11]. TMR devices have also been proposed for next-generation read sensors in magnetic disk drives [12].

Most of the interest for applications currently centres on systems with amorphous aluminium oxide tunnelling barriers because of the relative ease of growing adherent aluminium oxide without pinholes. Unfortunately, these systems are difficult to characterize and model because of the noncrystalline or amorphous nature of the oxide and the lack of any known epitaxial relationship between the oxide and the ferromagnetic electrodes. Much larger magnetoresistances have been predicted in recent calculations on epitaxial spin tunnelling systems [13–18].

In this review we shall concentrate on the developments of the theory of spin-dependent tunnelling, emphasizing spin-dependent tunnelling through interfaces that are sufficiently well characterized that their detailed electronic structure can be understood and calculated. We shall begin, however, with a survey of simple models that have been applied to spin-dependent tunnelling, including the much used Julliere model [3]. We shall show that the notion of the polarization of the Fermi energy density of states (DOS) of the electrodes on which this model is based should be replaced by the concept of the polarization of the transmission probability of the electrode–barrier interface. We shall then describe more detailed approaches that are able to treat the underlying electronic structure of spin tunnelling junctions more realistically and show how this electronic structure determines the TMR. This will be illustrated primarily with examples from our own work. We conclude with a summary of our current understanding of spin-dependent tunnelling and of the many important aspects that are still not fully understood.

1.1. Landauer formula

In this subsection we introduce the Landauer formalism for electron transport which relates the conductance of a sample to the probabilities of electron transmission and reflection [19, 20]. To understand the Landauer conductance formula it is helpful to consider two reservoirs of electrons connected by a sample as shown in figure 1. For our application, the sample would consist of the tunnelling barrier surrounded by the two electrodes. If we imagine the left-hand reservoir, with chemical potential μ_1 and distribution function $f(\mu_1)$, to be an emitter of right going electrons, we can write the current density of those electrons that leave the reservoir on the left and enter the reservoir on the right in terms of the transmission probability $T^{++}(\mathbf{k}, \mathbf{k}')$ as

$$J^+ = \frac{e}{(2\pi)^3} \int \mathrm{d}^3k \; v_z^+(\mathbf{k}) f(\mu_1) \sum_{k'} T^{++}(\mathbf{k}, \mathbf{k}'), \tag{1}$$

where $+z$ is the direction from reservoir 1 to reservoir 2, and the superscripts + indicate that the electrons are travelling in the $+z$ direction. The parallel and perpendicular components of $\mathbf{k}$ are $\mathbf{k}_\parallel$ and k_z, respectively. Performing the integral over k_z yields

$$J^+ = \frac{e}{A}\sum_{\mathbf{k}_\parallel, j;\mathbf{k}'} \frac{1}{2\pi}\int \mathrm{d}k_z \,\frac{1}{\hbar}\frac{\partial \varepsilon}{\partial k_z} f(\mu_1) T^{++}(\mathbf{k}, \mathbf{k}'), \tag{2}$$

which yields an expression for the current,

$$I^+ = \frac{e}{h}\int^{\mu_1} \mathrm{d}\varepsilon \sum_{\mathbf{k}_\parallel, j;\mathbf{k}'_\parallel, i} T^{++}(\mathbf{k}_\parallel, j; \mathbf{k}'_\parallel, i), \tag{3}$$

where we have assumed that the scattering by the sample is elastic or nearly so in order that $\mathbf{k}$ and $\mathbf{k}'$ are at approximately the same energy ϵ. Here, $\mathbf{k}_\parallel$ ($\mathbf{k}'_\parallel$) are the components of $\mathbf{k}$ ($\mathbf{k}'$) in the xy plane, and the band indices i, j are needed because there is generally more than one Bloch state for a given value of $\mathbf{k}_\parallel$. A line of reasoning similar to the one that led to equation (3) leads to an expression for the current of electrons emitted in the $-z$ direction by the reservoir on the right which enter the reservoir on the left,

$$I^- = \frac{e}{h}\int^{\mu_2} \mathrm{d}\varepsilon \sum_{\mathbf{k}_\parallel, j;\mathbf{k}'_\parallel, i} T^{--}(\mathbf{k}_\parallel, j; \mathbf{k}'_\parallel, i). \tag{4}$$

At this point, one usually equates T^{++} and T^{--} by invoking a symmetry argument such as time reversal symmetry. However, we note here that the transmission probabilities $T^{++}(\mathbf{k}_\parallel, j; \mathbf{k}'_\parallel, i)$ and $T^{--}(\mathbf{k}'_\parallel, i; \mathbf{k}_\parallel, j)$ are generally not equal when the electrode Fermi surfaces do not have mirror symmetry. This is most easily seen for the case of specular transmission for which $k_\parallel$ is conserved. In this case, time reversal states that $T^{++}(k_\parallel, k_z, k'_z) = T^{--}(-k_\parallel, -k'_z, -k_z)$, but this is not the same as $T^{--}(k_\parallel, -k'_z, -k_z)$ unless the Fermi surfaces of the electrodes have mirror symmetry. This was emphasized in [21] for tunnelling through a molecule. Another very common example is transport perpendicular to the (111) planes of an fcc material such as copper. Instead of using time reversal symmetry, a correct and equally effective argument can be constructed based on the requirement that in equilibrium there should be no net current at each energy level summed over all bands, thus,

$$\sum_{\mathbf{k}_\parallel, j;\mathbf{k}'_\parallel, i} T^{++}(\mathbf{k}_\parallel, j; \mathbf{k}'_\parallel, i) = \sum_{\mathbf{k}_\parallel, j;\mathbf{k}'_\parallel, i} T^{--}(\mathbf{k}_\parallel, j; \mathbf{k}'_\parallel, i). \tag{5}$$

This allows us to write the net current for a sufficiently small voltage as

$$I = I^+ - I^- = \frac{e^2}{h}\sum_{\mathbf{k}_\parallel, j;\mathbf{k}'_\parallel, i} T^{++}(\mathbf{k}_\parallel, j; \mathbf{k}'_\parallel, i)\frac{\mu_1 - \mu_2}{e}, \tag{6}$$

which yields the Landauer conductance formula,

$$G = \frac{e^2}{h}\sum_{\mathbf{k}_\parallel, j;\ \mathbf{k}'_\parallel, i} T(\mathbf{k}_\parallel, j; \mathbf{k}'_\parallel, i). \tag{7}$$

This can be further simplified if the electrode and tunnelling barrier system has translational symmetry in the plane parallel to the interface so that the transmission conserves $\mathbf{k}_\parallel$. In this case, the transmission probability has the form

$$T(\mathbf{k}_\parallel, j; \mathbf{k}'_\parallel, i) = T(\mathbf{k}_\parallel, j, i)\delta_{\mathbf{k}_\parallel \mathbf{k}'_\parallel}, \tag{8}$$

and the conductance is given by

$$G = \frac{e^2}{h}\sum_{\mathbf{k}_\parallel, j, i} T(\mathbf{k}_\parallel, j, i). \tag{9}$$

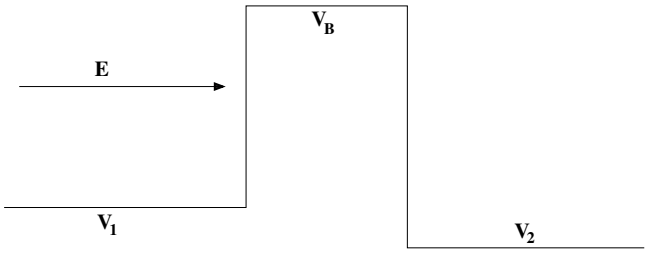

Figure 2. Free electrons incident on a simple barrier.

The original Landauer formula has the ratio of transmission probability divided by reflection probability (T/R) where we have only the transmission probability in equation (9). It is argued that this additional factor of $1/R$ arises from the reflected electrons changing the chemical potential of the reservoirs. It is now usually accepted that this additional factor of $1/R$ is present or not depending on exactly how the measurement is performed, that is, on whether or not one measures current and voltage using the same leads, as is assumed in the derivation here, or whether a separate set of probes is used to determine the voltage across the sample. When applied to tunnelling, the difference between the two formulae will usually be negligible because tunnelling transmission probabilities are usually very small and the reflection probabilities are near unity.

2. Free electron model

The Landauer formula is often discussed in terms of a model in which free electrons are incident on a simple repulsive step potential (figure 2). For a single spin channel, the potentials in the three regions are V_1, V_B, and V_2, respectively, where $V_1 < E_F$, $V_2 < E_F$, and $V_B > E_F$. Depending on the spin alignment, V_1 and V_2 are taken to be either $V_\uparrow$ or $V_\downarrow$. In this model, the exchange splitting is given simply by $V_\uparrow - V_\downarrow$. The z component of the wavevector for an electron at the Fermi level on the left of the barrier is $k_1 = \sqrt{(2m/\hbar^2)(E_F - V_1 - k_\parallel^2)}$, and that on the right of the barrier is $k_2 = \sqrt{(2m/\hbar^2)(E_F - V_2 - k_\parallel^2)}$. Inside the barrier the wavefunction is a linear combination of exponentially growing and decaying wavefunctions with wavevector, $\kappa = \sqrt{(2m/\hbar^2)(V_B - E_F + k_\parallel^2)}$. The unitary transmission coefficient for this barrier is given by

$$T(k_\parallel) = \frac{16k_1\kappa^2k_2\exp(2d\kappa)}{\{\kappa(k_1+k_2)[1+\exp(2d\kappa)]\}^2 + \{(\kappa^2 - k_1k_2)[1-\exp(2d\kappa)]\}^2} \tag{10}$$

where d is the barrier thickness. The reflection coefficient, R, is $1 - T$. For most tunnelling situations, T is small, and R is close to unity. In this limit, we find that T is given by

$$T(k_\parallel) = \frac{16k_1\kappa^2k_2\exp(-2d\kappa)}{[\kappa(k_1+k_2)]^2 + (\kappa^2 - k_1k_2)^2}. \tag{11}$$

The tunnelling conductance per spin channel is given by equation (9), assuming that there is no diffuse scattering in the barrier region and consequently $\mathbf{k}_\parallel$ is conserved so that each $\mathbf{k}_\parallel$ is an independent conduction channel.

In order to apply the free electron model to spin-dependent tunnelling, we assume that the two spin channels are displaced in energy by $V_\uparrow - V_\downarrow$ and thus have different wavevectors,

$k_\uparrow = \sqrt{E_F - V_\uparrow - k_\parallel^2}$ and $k_\downarrow = \sqrt{E_F - V_\downarrow - k_\parallel^2}$, at the Fermi level. Thus, for example, if we assume the same ferromagnetic material on both sides of the barrier, the majority conductance for parallel alignment of the moments on opposite sides of the barrier is found from equations (3) and (5) using $k_1 = k_2 = k_\uparrow$, and for the minority conductance $k_1 = k_2 = k_\downarrow$, while the conductance for anti-parallel alignment of the moments is obtained by setting $k_1 = k_\uparrow, k_2 = k_\downarrow$.

2.1. Julliere model

A model that has been widely used to describe spin-dependent tunnelling was proposed by Julliere in his very short but much cited 1975 paper [3]. Julliere's model for spin-dependent tunnelling has been applied quite generally, not just to free electron systems, but it is instructive to discuss his model first in the context of this simple model.

The Julliere expression for the TMR follows immediately from the often-used assumption that the tunnelling probability is proportional to the product of the Fermi energy densities of states in the electrodes on either side of the barrier. Thus if the electrode polarization, P, is defined in terms of the majority ($n^\uparrow$) and minority ($n^\downarrow$) Fermi energy densities of states as

$$P = \frac{n^\uparrow - n^\downarrow}{n^\uparrow + n^\downarrow}, \qquad \frac{n^\uparrow}{n^\downarrow} = \frac{1+P}{1-P}, \tag{12}$$

then the TMR, i.e. the ratio of the change in conductance (when the moments are moved from antiparallel to parallel) to the conductance for anti-parallel moments can be written as

$$\frac{G_P - G_A}{G_A} = \frac{(n_1^\uparrow n_2^\uparrow + n_1^\downarrow n_2^\downarrow) - (n_1^\uparrow n_2^\downarrow + n_1^\downarrow n_2^\uparrow)}{n_1^\uparrow n_2^\downarrow + n_1^\downarrow n_2^\uparrow} = \frac{2P_1P_2}{1 - P_1P_2}. \tag{13}$$

This formula has been widely used for rationalizing experiments.

The values of electrode polarization, P, are often obtained from the analysis of superconducting tunnelling experiments. It is clear, however, that P obtained in this way does not measure the relative density of majority and minority states at the Fermi energy. The values of P measured experimentally [22, 23] for Fe, Co, and Ni, for example, indicate that the tunnelling in all three cases is dominated by majority electrons. If one believes the Julliere model, equation (13), this would contradict what is known about the electronic structure of these materials, particularly of Ni and Co for which electronic structure calculations indicate an order of magnitude larger minority Fermi energy DOS than majority. There have also been attempts to correlate P with the difference in the numbers of majority and minority electrons, i.e. the number of Bohr magnetons per atom. We believe that any experimental correlation of this type must be coincidental because tunnelling, at least for low bias, involves electrons near the Fermi energy.

If we apply the Julliere model to the simple barrier model for free electrons depicted in figure 2, the polarizations, P_1 and P_2, that enter equation (13) are given simply as

$$P_1 = \frac{k_1^\uparrow - k_1^\downarrow}{k_1^\uparrow + k_1^\downarrow} \qquad P_2 = \frac{k_2^\uparrow - k_2^\downarrow}{k_2^\uparrow + k_2^\downarrow}, \tag{14}$$

where $k_i^{\uparrow\downarrow}$ represent the majority and minority Fermi momenta for the two electrodes. Figure 3 shows the calculated TMR as a function of the polarization of the electrons at the Fermi energy in the simple barrier model [24]. The calculations assume a barrier height of 0.25 eV and thicknesses ranging from 5 to 200 Å. The curve marked J is the Julliere result, equation (13). It is clear that the Julliere model is not a good representation of the TMR when applied in this way.

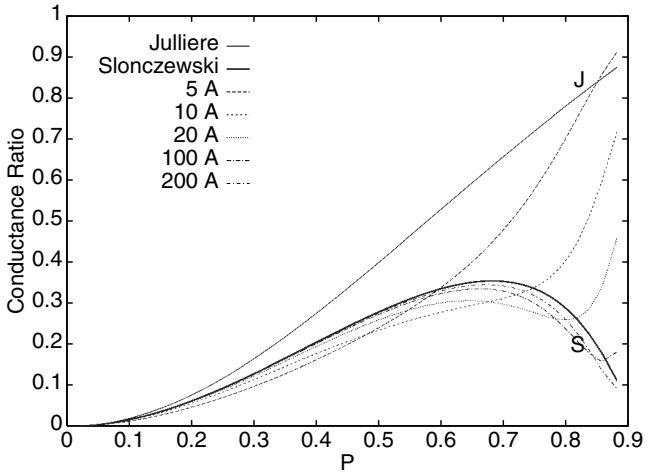

Figure 3. Conductance ratio for the spin-dependent tunnelling of a free electron at energy $E_F = 6.8$ eV and for a barrier height at 0.25 eV above E_F. Barrier widths of 5, 10, 20, 100, and 200 Å are shown along with the Julliere and Slonczewski results labelled by (J) and (S) respectively.

The curve labelled 'S' in figure 3 shows the result of an alternative expression for the TMR due to Slonczewski [25] who noted that the expression for the free electron model calculated in the limit of thick barriers using equations (11) and (9) could be expressed in the Julliere form, equation (13) if he used, not the true polarization at the Fermi energy DOS, but an effective polarization defined by

$$P_{\text{eff}} = P\frac{\kappa_0^2 - k^{\uparrow}k^{\downarrow}}{\kappa_0^2 + k^{\uparrow}k^{\downarrow}}, \tag{15}$$

where $\kappa_0 = \sqrt{(2m/\hbar^2)(V_B - E_F)}$ describes the rate of decay of the wavefunction for $k_{\parallel} = 0$ in the barrier region. It can be seen that Slonczewski's result represents the TMR fairly well for sufficiently thick barriers.

2.2. Generalized Julliere model

Since Slonczewski showed that the Julliere expression for TMR is valid for thick barriers if one uses a different definition of the polarization, it is interesting to ask the question of whether this result is more general. Is there a definition of the 'polarization' that makes the Julliere expression valid? In order to answer that question, let us explore what Slonczewski's effective polarization really means.

To do that, let us consider one-half of the transmission through a simple barrier problem as shown in figure 4, i.e. electrons incident on a step function barrier. The wavefunctions for unit incident flux are given by

$$\begin{aligned}\psi(x < 0) &= \frac{\exp(\mathrm{i}kx) + r\exp(-\mathrm{i}kx)}{\sqrt{k}}\\ \psi(x > 0) &= \frac{t\exp(-\kappa x)}{\sqrt{\kappa}}.\end{aligned} \tag{16}$$

The reflection probability in this case is unity for all values of $\mathbf{k}_{\parallel}$, and the transmission probability must be zero if one uses the usual definition of the transmission probability based

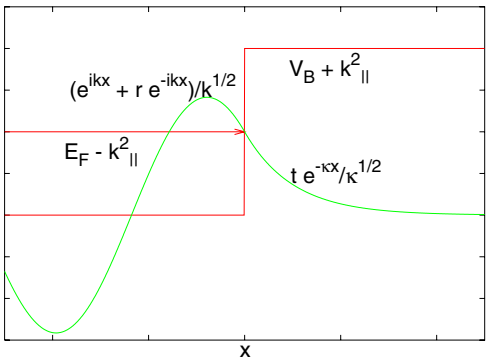

Figure 4. Transmission probability for an evanescent wave at an interface.

on the transmitted flux. However, the wavefunction is not zero within the barrier. Thus the probability for finding an electron on the right-hand side of the interface is $T\exp(-2\kappa x)$, with

$$T = \frac{4k\kappa}{k^2+\kappa^2}. \tag{17}$$

Thus T can be considered to be a generalized transmission probability through a electrode–barrier interface at $x = 0$.

Returning to the expression for the tunnelling probability for a barrier sufficiently thick that $\exp(-2\kappa d) \ll 1$ (given by equation (11)), we find that the probability for transmission through the barrier can be written as the product of the probability for transmission across each of the interfaces times a factor that describes the exponential decay of the electron probability in the barrier,

$$T_{\mathrm{B}}(\mathbf{k}_\parallel) = T_{\mathrm{L}}(\mathbf{k}_\parallel)T_{\mathrm{R}}(\mathbf{k}_\parallel)\exp(-2\kappa d). \tag{18}$$

Here T_{B} is the transmission probability through the barrier. T_{L} and T_{R} are the probabilities for an electron to be transmitted across the left and right electrode–barrier interfaces respectively, as given by equation (17). Because $\kappa^2 = \frac{2m}{\hbar^2}(V_{\mathrm{B}} - E_{\mathrm{F}} + k_\parallel^2)$, it will primarily be the $\mathbf{k}_\parallel = 0$ states that contribute to the conductance. Slonczewski's effective polarization (equation (15)) is simply related to this single interface transmission probability through

$$P_{\mathrm{eff}} = \frac{T^\uparrow - T^\downarrow}{T^\uparrow + T^\downarrow} = P\frac{\kappa_0^2 - k^\uparrow k^\downarrow}{\kappa_0^2 + k^\uparrow k^\downarrow}, \tag{19}$$

where P_{eff}, $T^\uparrow$, and $T^\downarrow$ refer to either the right or left interface. Note that this yields a Julliere-like result for the TMR of a simple barrier, but the meaning of the polarization that enters is completely different from the usual interpretation. The 'polarization' really refers to the relative probability of an up- or down-spin electron being transmitted from an electrode into the barrier as an evanescent wave. It depends both on the electrode and on the barrier.

Currently, most applications of TMR involve amorphous aluminium oxide barriers. For this type of barrier, it is clear that $\mathbf{k}_\parallel$ will not be conserved because the disorder breaks the two-dimensional translational invariance parallel to the plane of the interfaces. The amorphous barrier is difficult to treat, but we can understand an only slightly less complicated problem, one in which the interfaces are strongly disordered, but the barrier itself is ordered. In this case it is likely that the probability for transmission through the barrier can still be approximately factorized in the case where $T \ll 1$. In this case, however, the important quantity is the diffuse transmission probability for an electron to scatter at the left-hand interface from $(\mathbf{k}_\parallel, i)$ on the

left to $(0, j)$ in the barrier (and the reverse at the other interface), where $(0, j)$ is the slowest decaying state in the barrier.

Thus the conductance will be given by equation (7) where the transmission probability can be written in a factorized form,

$$T(\mathbf{k}_\parallel, i; \mathbf{k}'_\parallel, l) = T_{\mathrm{L}}(\mathbf{k}_\parallel, i; 0, j) T_{\mathrm{R}}(0, j, \mathbf{k}'_\parallel, l) \exp[-2\kappa(0, j)d]. \tag{20}$$

Thus a Julliere-like formula for the conductance may apply where the concept of electrode polarization is replaced by an averaged interfacial transmission polarization defined by

$$P = \frac{\langle T^\uparrow \rangle - \langle T^\downarrow \rangle}{\langle T^\uparrow \rangle + \langle T^\downarrow \rangle} \tag{21}$$

where, for example,

$$\langle T^\uparrow \rangle = \sum_{\mathbf{k}_\parallel, i} \langle T^\uparrow(\mathbf{k}_\parallel, i; 0, j) \rangle. \tag{22}$$

When considering the validity and utility of the Julliere model, it is important to take into account the system to which it is applied. Julliere was quite aware of the work of Meservey and Tedrow [4, 22] who had investigated the spin dependence of tunnelling between Al and various ferromagnetic electrodes. The barrier layer in these tunnelling experiments was typically an aluminium oxide that formed on the aluminium layer before deposition of the ferromagnetic layer. The superconducting tunnelling experiments were interpreted in terms of a model in which the tunnelling conductance in each spin channel was assumed to be proportional to the product of the densities of states in the ferromagnet and in the superconducting Al. Based on this assumption, the 'polarizations' of the electrons at the Fermi energy in the ferromagnet would be obtained by fitting to the tunnelling current–voltage curve. In actuality, we speculate that what was being determined as a DOS polarization was actually much closer to the averaged transmission probability polarization of equation (22). Indeed, it was clear to Tedrow and Meservey as well as to Julliere that the measured quantity they called P had the opposite sign from what would have been expected for the polarization of the Fermi energy DOS of cobalt or nickel. This may have led to the unfortunate identification of P with the magnetic moment [22].

The conditions for the application of the Julliere expression for the TMR then are the following.

(a) The tunnelling barrier must be sufficiently thick that the transmission probability is very small.

(b) The averaged interfacial transmission polarization must be determined for the electrode–barrier combination under consideration.

Since many TMR experiments involve tunnelling barriers made of oxidized aluminium, and since the values of P are also usually determined using an oxidized aluminium barrier, it may be possible to carefully check the version of the Julliere model described here by carefully preparing the electrode barrier interfaces so that they have identical structures in the TMR devices and in the superconducting tunnel junctions. The polarization values quoted in the literature vary significantly depending on the precise conditions of sample preparation and data analysis. It is interesting to note that the Tedrow–Meservey polarizations derived from aluminium oxide barriers would not have been appropriate for the Fe–Ge–Co junctions discussed in Julliere's paper.

2.3. *Effects of lateral symmetry*

One characteristic of the free electron model is that it predicts a single decay rate for given values of $\mathbf{k}_\parallel$ and energy. That is, the tunnelling current should decay with the barrier thickness, d, as $\exp(-2\kappa d)$ where $\kappa = \sqrt{(2m/\hbar^2)(V_B - E) + k_\parallel^2}$. It was recently pointed out [26] that this is incorrect for realistic leads. Even if the potential in the barrier region is constant, the wavefunctions in the barrier region must still match the wavefunctions in the electrodes and these will typically have various symmetries. If the boundary conditions at the edge of the barrier can be matched with the separable form $\psi(x, y, z) = \phi(x, y)\exp(-\kappa z)$ where the variation of the lateral part of the wavefunction ϕ is assumed to be oscillatory, then the decay perpendicular to the barrier ($k_\parallel = 0$) will be given by

$$\kappa^2 = \frac{2m}{\hbar^2}(V_B - E) - \frac{\langle\phi|(\frac{\partial^2}{\partial x^2} + \frac{\partial^2}{\partial y^2})|\phi\rangle}{\langle\phi|\phi\rangle}. \tag{23}$$

The second term is positive and correlates with the number of nodes of $\phi(x, y)$. It contributes to an additional increase in the rate of decay perpendicular to the interface (just as a non-zero value of $k_\parallel$ would). In this picture, the role of symmetry is to determine the number of nodes of the wavefunction in the plane of the interface. This translates into curvature in this plane which affects the decay rate. States that are primarily s-like will have little of this curvature, p-like states will have more and d-like states will typically have even more. For this reason, we argue that the result that the nature of the state in the electrode influences its decay rate in the barrier is quite general. Most of the d-derived states, in particular, will be disadvantaged in penetrating the barrier because of their higher curvature due to additional nodes in the plane parallel to the barrier.

The actual decay rates have been calculated [26] directly from the layer Korringa–Kohn–Rostoker (LKKR) code [27]. In figure 5 we show one such calculation for the tunnelling probability of electrons from Fe(100) leads into a vacuum barrier at the Fermi energy of bulk Fe. Vacuum is approximated here by a spatially homogeneous barrier. In order to see the decay rates within the barrier layer, we calculate the charge density on each lattice site, i.e., the modular square of the wavefunction integrated over the atomic sphere, due to a single wavefunction at the Fermi energy, with the boundary condition that there is a unit flux of incident electrons in a single Bloch state on one side (left-hand side in this case) plus reflected electrons on the same side (left) and transmitted electrons on the opposite side (right). These boundary conditions yield a partial DOS that decays in the barrier from left to right which we call the 'tunnelling density of states' (TDOS).

The results displayed in figure 5 show three decay rates. The majority Δ_1 state (which contains s, p, and d components with 1, z, and $2z^2 - x^2 - y^2$ symmetries respectively) decays as $\kappa = \sqrt{(2m/\hbar^2)(V - E)}$, exactly as expected for the simple barrier model. The other states, however, decay more rapidly. The minority Δ_2 (d character, $x^2 - y^2$ symmetry) and all of the Δ_5 states (p and d components with x, y, xz and yz symmetries) decay as $\kappa = \sqrt{(2m/\hbar^2)(V - E) + g_1^2}$ where $g_1 = 2\pi/a$ for a square lattice of lattice constant a. The majority and minority $\Delta_{2'}$ states that have d character and xy symmetry decay as $\kappa = \sqrt{(2m/\hbar^2)(V - E) + g_2^2}$ with $g_2 = \sqrt{2}(2\pi/a)$. g_1 and g_2 are simply the magnitudes of the first two reciprocal lattice vectors of the two-dimensional lattice parallel to the interfaces. These decay rates match perfectly with the number of nodes and the periodicity of the corresponding wavefunctions in the xy plane.

For the case of $\mathbf{k}_\parallel \neq 0$, the symmetry of the Bloch states and of the decaying evanescent states that they couple to becomes more complicated. The wavefunction in the barrier region

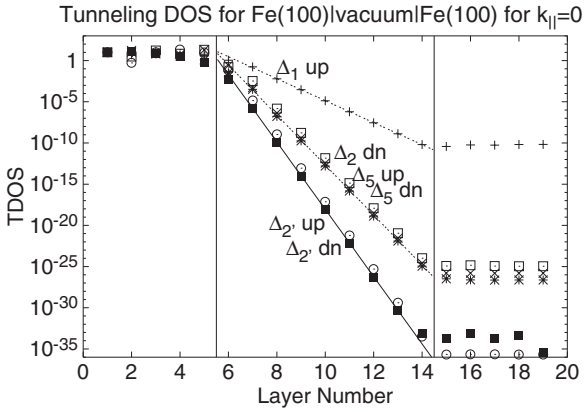

Figure 5. Tunnelling DOS for $k_\parallel = 0$ for Fe(100)|vacuum|Fe(100) calculated using scattering boundary conditions with Bloch waves incident from the left. The straight lines have slopes given by $-2\sqrt{(2m/\hbar^2)(V_B - E_F) + g^2}$ as described in the text. The Δ_2 minority, Δ_5 majority and minority states are numerically indistinguishable, and likewise for the $\Delta_{2'}$ states of both majority and minority spins. The moments of the two iron electrodes are assumed to be aligned.

that joins to the incident plus reflected Bloch wave on the left usually becomes a mixture of different symmetry states, and can be expanded in terms of reciprocal lattice vectors in the form [13]

$$\psi(\rho, z) = \sum_g c_g e^{i(\mathbf{k}_\parallel + \mathbf{g})\cdot\rho - \sqrt{(2m/\hbar^2)(V_B - E) + (\mathbf{k}_\parallel + \mathbf{g})^2} z}. \tag{24}$$

Here ρ is a vector in the xy plane and we have taken the limit of a thick barrier so that growing evanescent waves are excluded. The transmission coefficient for thick barriers will then depend on the magnitude of the $g = 0$ coefficient of the wavefunction expansion in equation (24). Note that this component of the wavefunction corresponds to a probability density, $P(\rho, z) = |\psi(\rho, z)|^2$, that is constant in the xy plane. Coefficients for the wavefunction in the barrier with $g \neq 0$ will be necessary for the probability density to join continuously to that of the metal.

Most d-components of the wavefunction will have nodes in the xy plane and will therefore generate only very small contributions to the $g = 0$ expansion coefficients. This means that the d component of the TDOS will decay very rapidly in the first few layers of the barrier and that the contribution to the transmission of Bloch states that have d-derived oscillations in the xy plane will typically be several orders of magnitude smaller than that of Bloch states that do not have such oscillations. Even for bands that do not contain the Δ_1 component at $\mathbf{k}_\parallel = 0$, the wavefunctions will have some Δ_1 component at $\mathbf{k}_\parallel \neq 0$. Thus, after some initial rapid decay, all wavefunctions will eventually decay at the same rate (but at a much lower level) if the barrier is sufficiently thick. This is illustrated in figures 6 and 7 which show the TDOS for the same boundary conditions as figure 5. In this case, however, $\mathbf{k}_\parallel = (0.036, 0.018)$ and we show the angular momentum decomposition of the TDOS. In the barrier, the angular momentum decomposition is performed around fictitious sites that would form a continuation of the bcc Fe(100) lattice. Figure 6 shows the TDOS for the continuation of the majority Δ_1 band at $\mathbf{k}_\parallel = (0, 0)$ to $(0.036, 0.018)$. The calculated TDOS is essentially unchanged for this Bloch state which does not have rapid oscillations in the xy plane. The TDOS for the other Bloch states is, however, affected by the loss of symmetry as is shown in figure 7. There is an initial rapid decay of the TDOS as the parts of the wavefunction that have in-plane oscillations

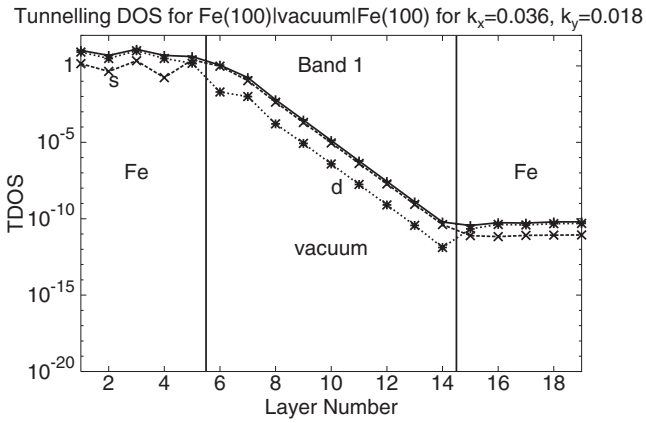

Figure 6. Tunnelling DOS for $\mathbf{k}_\parallel \neq 0$ for Fe(100)|vacuum|Fe(100) for the Bloch state that has Δ_1 symmetry at $\mathbf{k}_\parallel = 0$. The total (+) and the s ($\times$) and d ($*$) partial DOSs are plotted. These calculations employ the same boundary conditions as figure 5.

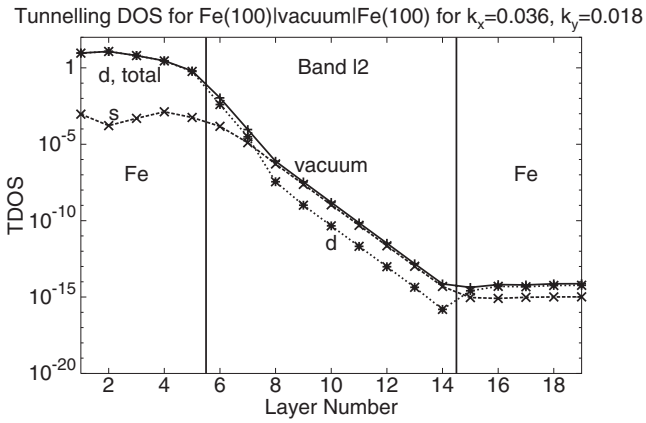

Figure 7. Tunnelling DOS for $\mathbf{k}_\parallel \neq 0$ for Fe(100)|vacuum|Fe(100) for a Bloch state that has no $g = 0$ component at $\mathbf{k}_\parallel = 0$. The total (+) and the s ($\times$) and d ($*$) partial DOS are plotted. These calculations employ the same boundary conditions as figures 5 and 6.

decay according to equation (24) with $g \neq 0$. After those terms are gone there is a small residual component that decays at the rate given by equation (24) with $g = 0$.

2.4. Simple models not adequate for spin dependent tunnelling

Although the simple models that we have presented in the present section are instructive, we shall show in later sections that they are insufficient for understanding some of the important phenomena that are predicted to occur in realistic systems. Despite common assumptions we shall see that neither the bulk DOS of the electrodes nor the interfacial DOS is the critical factor in determining the tunnelling rate or the TMR.

As we will see from the first-principles calculations described in later sections, each band couples to the barrier evanescent states differently, hence their contributions to tunnelling current differ by orders of magnitude. In addition, the free electron model fails to account for

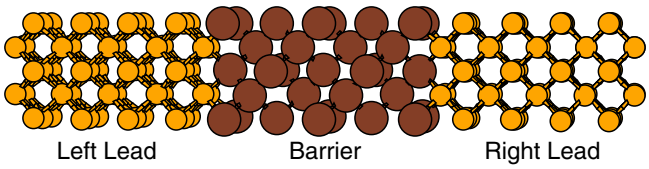

Figure 8. The system consists of a barrier layer sandwiched between two semi-infinite leads. The system is assumed to be periodic in the directions parallel to the interfaces.

the difference in the lateral symmetry of the Bloch wavefunctions at the same $\mathbf{k}_{\|}$ which can lead to different decay rates in the barrier. We will also demonstrate other aspects of spin-dependent tunnelling that are generally missed by simple models. These include the complex bands in the barrier layer, the interface resonance states, and a strong chemical bond effect.

The simple models of electron tunnelling had their origins in semiconductor physics. For most semiconductors, the free electron model works very well. One often only needs to provide effective masses and band offsets to reasonably describe a semiconductor junction. In spin transport systems, because of the critical role of the d-band electrons, one cannot rely on the simple model. Instead, first-principles studies have become a crucial part of the theoretical understanding.

3. Self-consistent band structure for interfaces

The first step in calculating the tunnelling conductance must be the calculation of the proper self-consistent DOS of the metal–insulator–metal system. There are many first-principles methods for treating interface structures. However, approaches which treat the semi-infinite leads with the correct boundary conditions are most useful because they allow the computation of transmission and reflection amplitudes of Bloch waves for tunnelling junctions [13–16, 28, 29]. Although supercell calculations of the electronic structure of spin tunnelling junctions have been performed, it is difficult to use them to calculate transport coefficients. In our discussion in this paper we will focus on our own results using the LKKR technique [27]. Results obtained by other first-principles methods are generally similar to ours. The LKKR method is a self-consistent electronic structure method, based upon the local spin-density approximation, or some other approximation to density functional theory, which can evaluate the electronic structure of a three-dimensional solid without requiring the usual constraint of three-dimensional translational symmetry. The extended solid is viewed as one composed of an infinite stack of planes of atoms, each of which has two-dimensional translational symmetry. Thus the method is ideally suited to the problem at hand, namely a system formed of two semi-infinite stacks of layers, which form the leads, on either side of the tunnel barrier (as shown schematically in figure 8).

Magnetism is treated within the local spin-density approximation, in which the spin up and spin down densities are allowed to converge independently. In this work the Perdew–Zunger [30] parametrized form of exchange–correlation potential was used. This approximation fits the energy for paramagnetic and fully polarized limits of Monte Carlo simulations of the homogeneous electron gas performed by Ceperley and Alder [31]. Values for intermediate polarizations were obtained from an interpolation formula derived by Vosko *et al* [32].

The calculation for an interface proceeds as follows. First a bulk calculation is performed to find the self-consistent potentials for the two leads on layers far from the barrier layer. Since,

in a metallic system, screening ensures that the electronic perturbations in the leads, due to the tunnel junction, will be localized spatially at the interface, atoms far from the barrier are assumed to have bulklike potentials whose values are those obtained from the corresponding bulk calculation. Then an interface containing the barrier layer is set up (figure 8). The Green function is used to embed barrier layers and additional atomic layers of the electrode (several on each side of the barrier layer) in the bulk electrode. The Fermi energy is maintained equal to that of the bulk lead as the self-consistent electronic structure is calculated for the entire system consisting of bulk lead plus the embedded layers. The spin up and spin down potentials on atomic layers within the barrier and within the leads near the interface are allowed to relax through the iterative procedure described above until electrostatic self-consistency is achieved throughout the system. The self-consistent calculation allows for a rearrangement of charge between the layers necessary to correctly offset the bands of the barrier layer relative to those of the electrode. Due to good screening in the metal leads, the self-consistently calculated potentials seldom differ significantly from those of the bulk if they are more than three or four layers from the interface; typically only three atomic layers of the electrodes on either side are included in the interface region for which the electron potential is relaxed.

In the remainder of this section, we will summarize the calculations of the electronic structure of several spin-dependent tunnelling systems. In these calculations, the electrodes were Fe[100] with various barrier layers. The lattice constant of each system was fixed to that for the experimental value of bulk bcc Fe, 2.866 Å, and no relaxation of the lattice was included unless otherwise noted.

3.1. Electronic structure of symmetric junctions

Most published calculations [13–18, 34–36] considered symmetric junctions, where both interfaces of the junction are the same. These calculations obtained very similar electronic structures for different barrier materials. Common features in the electronic structure that are seen from these calculations include a reduction of DOS at the Fermi energy in the majority spin channel, a sharp peak in the DOS and strong interface resonances near the Fermi energy in the minority spin channel, and sensitivity of the interface magnetic moment to the structure and the electronic structure at the interfaces. The calculations covered a range of barriers, including semiconductors Si, Ge, GaAs, and ZnSe, and insulator MgO, but were mostly limited to Fe leads. Only one study [34] considered the commonly used Al_2O_3 as barrier material (treated as an ordered phase); another [35] considered $SrTO_3$, but neither gave any conductance results.

Here we summarize the results for two junctions, Fe|ZnSe|Fe with a Zn terminated barrier layer, and Fe|MgO|Fe, with a focus on the latter, to highlight the role of electronic structure in determining tunnelling conductance and TMR. The tunnel junction formed from several [100] layers of ZnSe sandwiched between two semi-infinite stacks of Fe[100] layers is one of the first systems calculated by first-principles electronic structure approaches [13, 17, 36]. The lattice match between Fe[100] and several diamond and zinc-blende semiconductors is quite good. The lattice constant for bcc Fe is 2.87 Å, while those of Ge, GaAs, and ZnSe are 5.66, 5.65, and 5.67 Å, respectively. The lattice constants of the semiconductors are almost exactly twice that of Fe, leading to modest lattice mismatches of only about 1.4%. For Fe|ZnSe|Fe, fixing the lattice constant to that for bulk bcc Fe causes a slight isotropic expansion of all the ZnSe layers. In the case of the Fe|MgO|Fe junction, the lattice mismatch between Fe(100) and MgO(100) is slightly larger than for the semiconductors. In our calculations, the MgO lattice constant, both in plane and out of plane, was taken to be exactly a factor of $\sqrt{2}$ of that of the Fe, with the exception that the Fe–O distance was taken to be 2.16 Å. Detailed descriptions of these systems are found in [13] for Fe|ZnSe|Fe and [14] for Fe|MgO|Fe.

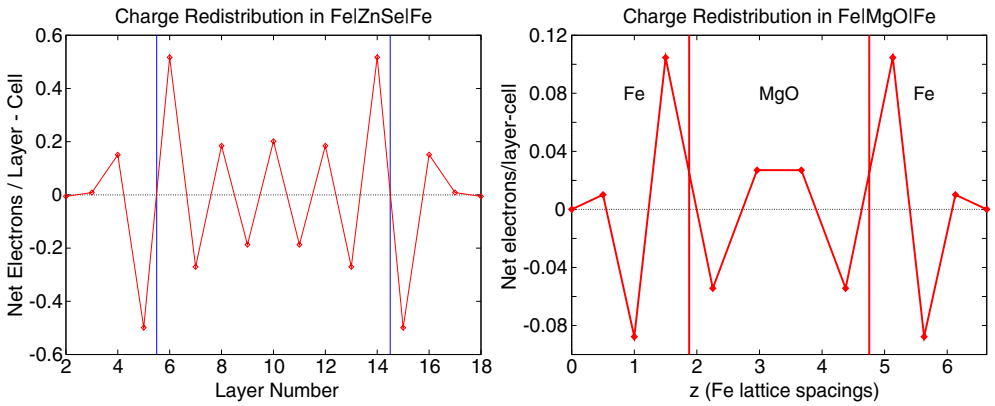

Figure 9. Charge redistribution near the barrier layer embedded in Fe for ZnSe [13] and MgO [14]. The redistribution of charge near the interface is necessary to correctly position (in energy) the barrier potentials relative to those of the Fe. Here it is assumed that the Zn layers are adjacent to the Fe.

The redistribution of net charges on each layer is shown in figure 9. A dipole layer forms at the interface as electrons are transferred from the Fe to the barrier layer in order to correctly position the Fermi energies of Fe and barrier layer. In the Fe|ZnSe|Fe case, there is also charge transfer within the ZnSe as electrons are transferred from Se to Zn layers. Reference [17] obtained a slightly different charge redistribution for this system. In particular, their result did not show the small oscillation of the charge in the first two Fe layers next to the interface. The origin of this small disagreement of about 0.1 electrons per atom is not clear. For the Fe|MgO|Fe junction we have counted the approximately 0.5 electrons in the empty sphere near the interface as residing on the last Fe layer. We find, in general agreement with the FLAPW calculations, that there is much smaller charge transfer between the Fe and the MgO. The total moment calculated for the iron atoms of the interfacial layer was approximately 3 μ_B which agrees with the FLAPW calculations cited previously [37].

The electronic DOS for Fe|MgO|Fe is shown in figures 10 and 11. The DOS near the interface is quite different from that of the bulk and the difference is opposite for the two spin channels. Near the interface, the majority DOS is strongly reduced in the vicinity of the Fermi energy, whereas for the minority spin channel the Fermi energy falls near a sharp peak in the DOS. The FLAPW calculations previously cited [37] also show a very sharp peak in the minority DOS for the case of a single Fe layer on MgO. The large peak in the minority DOS near the Fermi energy is localized on the atoms close to the interface and corresponds to an interface resonance which couples only weakly to the bulk Bloch states in the Fe leads. Also common to both the Fe|ZnSe|Fe and the Fe|MgO|Fe junctions, a significant DOS persists in the interior atomic layers of the barrier at the Fermi energy, especially for the minority channel.

Although it is tempting to explain the dramatic change in the DOS at the interface in terms of bonding between the interface Fe atoms and the atoms in the barrier layer, this is probably not the reason for the change. We have also observed similar changes in the DOS of the surface Fe layer in our calculation of the Fe(100)|vacuum interface [26]. The exchange splitting is different on the interfaces than in the bulk Fe, and is similar to the Fe surface. Thus the majority d levels at the interface are lower than in the bulk, leading to a reduction in the majority DOS at the interface. The magnetic moment at the interface is also significantly higher than the bulk, and is close to the value for the Fe surface. The large peak in the minority DOS near the

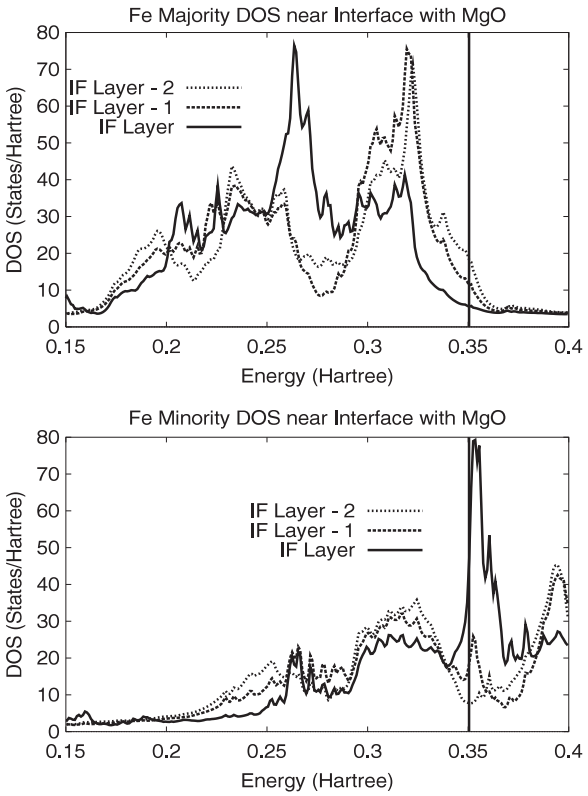

Figure 10. Density of states each atomic layer of Fe(100) near an interface with MgO. 1 hartree equals 27.2 eV.

Fermi level is probably due to the interface resonance states which will be discussed in later sections.

The small DOS in the gap of MgO on the interfacial MgO layer is due to the evanescent Fe states which decay exponentially into the MgO. The bandgap in ZnSe is much smaller than MgO. Using the potentials calculated for the central Zn and Se atomic layers to calculate the electronic structure of bulk ZnSe, it was found that it has a direct gap at the zone centre of 1.34 eV. This contrasts with the corresponding calculation for MgO, yielding a gap of 5.5 eV in [14], which agrees with previous DFT–LDA calculations [38] but is somewhat less than the experimental value of 7.8 eV [39]. The large difference in the bandgap will lead to orders of magnitude difference in the tunnelling conductance at the same layer thickness.

3.2. Electronic structure of Fe|FeO|MgO|Fe junctions

Because of the order of deposition, the two interfaces in a spin tunnel junction are usually asymmetric. This is typified by the Fe|MgO|Fe system, which was shown to actually contain an atomic layer of FeO on the bottom interface [40, 41]. Calculations of symmetric junctions tend to give very large TMR ratios. This contrasts sharply with the moderate TMR ratios measured experimentally. We have found [42] that part of this discrepancy may be due to the presence of the FeO layer on one of the interfaces.

The only difference in the structure of the Fe|FeO|MgO|Fe junction from that of the Fe|MgO|Fe junction is in the bottom interface which contains a single atomic layer of FeO.

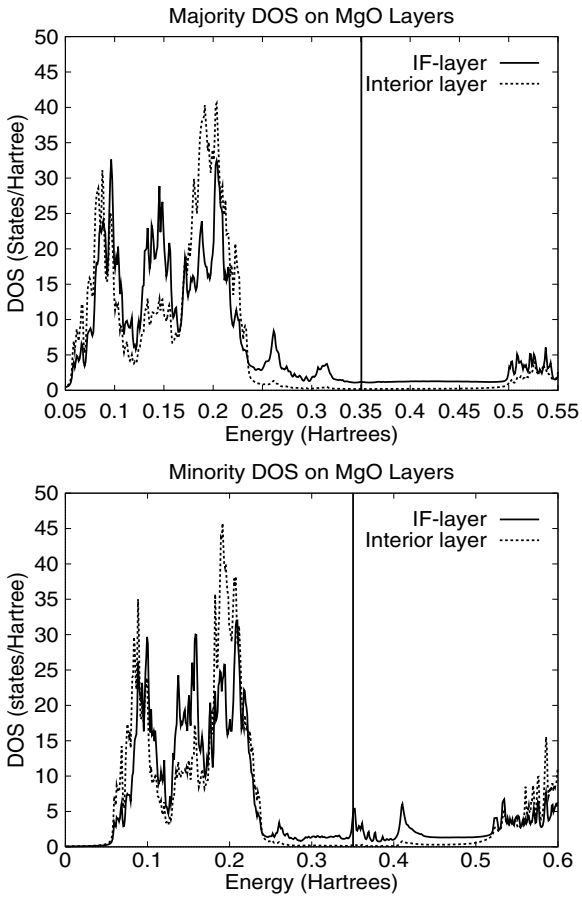

Figure 11. DOS for each of the atomic layers of MgO near an interface with Fe(100).

The Fe atom of this layer sits at the bcc site of the substrate Fe lattice. There is experimental evidence [41] that the oxygen sites are only about 60% occupied. The detail of the structure used in the calculation is explained in [42]. The self-consistent calculation is carried out in the same manner as in [14]. We limited our calculations within magnetic configuration space in the sense that all electron spins are assumed to be collinear. We also assumed that the magnetic order has the same periodicity as the two-dimensional lattice, thus disallowing antiferromagnetic ordering within the same atomic layer. Antiferromagnetic coupling between layers is allowed, however. In this section we show the electronic structure with 100% oxygen occupation on the FeO layer. In section 6.5 we will discuss the effect of partial oxygen occupancy in the FeO layer which is treated by the coherent potential approximation (CPA) [43]. We find, despite the large charge transfer between the Fe atom and the oxygen atom within the FeO layer, that the charge rearrangement necessary to correctly offset the bands of the MgO relative to those of Fe leads to very little charge transfer between layers, similar to the result we obtained for the Fe|MgO interface.

The calculated electronic DOS near the interface is very different from that of an Fe|MgO interface. Figure 12 shows the DOS for the Fe ASA spheres near the interface in the presence of the FeO layer. The most significant change is the almost complete disappearance of the d-band peak just below the Fermi energy for the Fe spheres on the FeO layer. The same peak

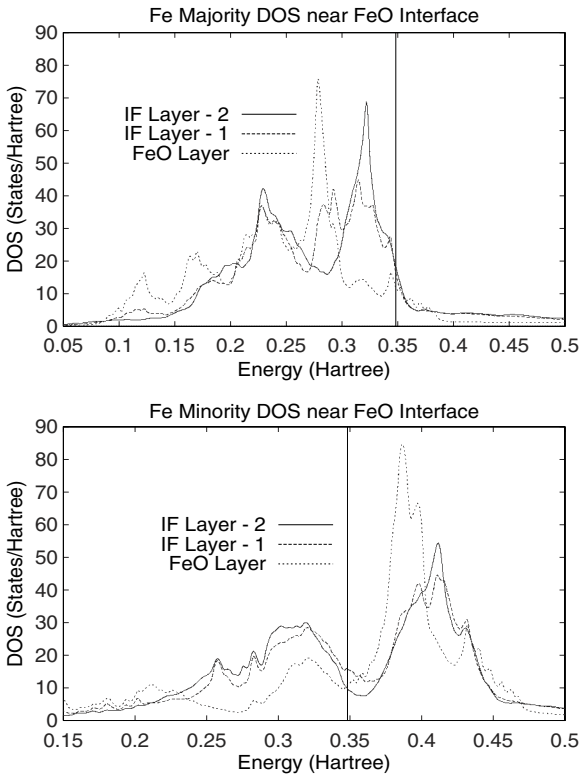

Figure 12. DOS for each Fe ASA sphere on the FeO layer and the Fe(100) layers near the interface. 1 Hartree equals 27.2eV.

is still present on the Fe layer at the Fe|MgO interface, though its height is greatly reduced. The sharp antibonding peak near the Fermi energy in the minority DOS of the Fe atom at the Fe|MgO interface is moved well above the Fermi energy when the interface is FeO. The oxygen DOS (figure 13) at the FeO layer shows a significant exchange splitting due to the strong hybridization with the Fe d electrons. In fact, the moment on the oxygen site is a significant 0.19 μ_B, and is parallel to the Fe moment.

The DOSs for the MgO atomic layers are shown in figure 14. A feature that was absent from the symmetric junctions is the relative shift of the MgO DOS between the layer next to the FeO layer and the interior layers. This is especially noticeable near the lower band edge around 0.1 hartree, where the effects of the hybridization with Fe d electrons is much less. This shift is not present when both sides of the MgO are Fe|MgO interfaces. The shift is due to the fact that the dipole due to the charge rearrangement on the interface is different for the Fe|FeO|MgO interface than for the Fe|MgO interface and can be viewed as a shift in the effective barrier potential from one side of the barrier to the other. This creates a difference in the offset of the barrier potential of about 0.055 hartree (or almost 1.5 eV) across the barrier layer, and it remains relatively unchanged as the barrier thickness is increased.

Both the strong hybridization of the Fe and O orbitals on the FeO layer, and the change in the effective barrier potential due to the dipole charge on the interfaces, can be expected to affect the tunnelling conductance. The former affects the coupling of d electrons from the Fe lead into the barrier; the latter affects the decay rate of the tunnelling current within the barrier.

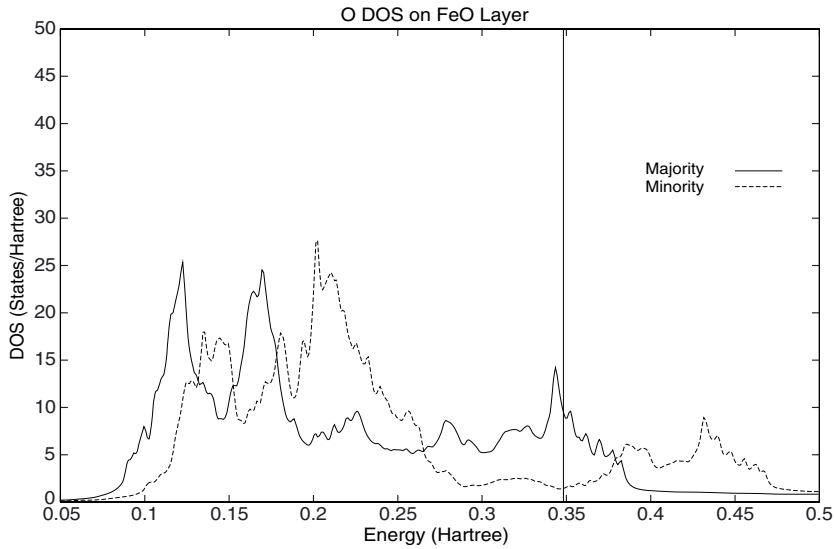

Figure 13. DOS for the oxygen ASA sphere on the FeO layer.

4. Transmission and reflection matrices for Bloch electrons

The calculation of the transmission and reflection matrices for Bloch electrons involves two steps. First one needs to calculate the bulk Bloch eigenstates within the left- and right-hand leads respectively. They can be obtained, for example, using the layer KKR code with the standard transfer matrix formulation [13]. Then a wavefunction matching scheme is used to solve the scattering problem of the Bloch electrons in the interface region [13, 28, 29]. Since the two leads may be different, calculations of the Bloch states are done for both the left- and the right-hand sides of the barrier. Each Bloch state at the Fermi energy corresponds to a channel in the Landauer–Büttiker formalism. Those states travelling towards the barrier correspond to incident channels while those travelling away from the barrier correspond to the scattered (transmitted or reflected) channels. These two subspaces will be used to define the scattering S matrix.

In addition to the band structure, it is necessary to compute the z component of the group velocity, v_z, so that the direction of travel of each eigenstate can be determined. This is found by noting that the eigenvalue $E(\mathbf{k})$ is an analytic function of the wavevector $\mathbf{k}$. Thus if a small imaginary part ΔE is given to the energy, the calculated value of k_z will also have a small imaginary part, Δk_z. The two are related by the velocity,

$$v_z = \frac{1}{\hbar}\frac{\partial E}{\partial k_z} \approx \frac{1}{\hbar}\frac{\Delta E}{\Delta k_z}. \tag{25}$$

The real part of k_z will be left unaltered, hence both k_z and v_z can be found simultaneously without having to resort to numerical differentiation of $E(\mathbf{k})$.

Because E is a periodic function of k_z, it follows that for a given value of $\mathbf{k}_\parallel$ there will be exactly as many states with positive v_z as with negative. The z component of the Bloch state's group velocity determines its direction of travel. Note that this is quite different from $\hbar k_z/m$. It is quite common to have a Fermi surface for which (for given $\mathbf{k}_\parallel$) there are two or four values of k_z that are greater than zero and none that are less than zero. If k_z were used to determine the direction of the Bloch wave's travel one would have the unphysical result that electrons with that value of $\mathbf{k}_\parallel$ could only propagate in one direction.

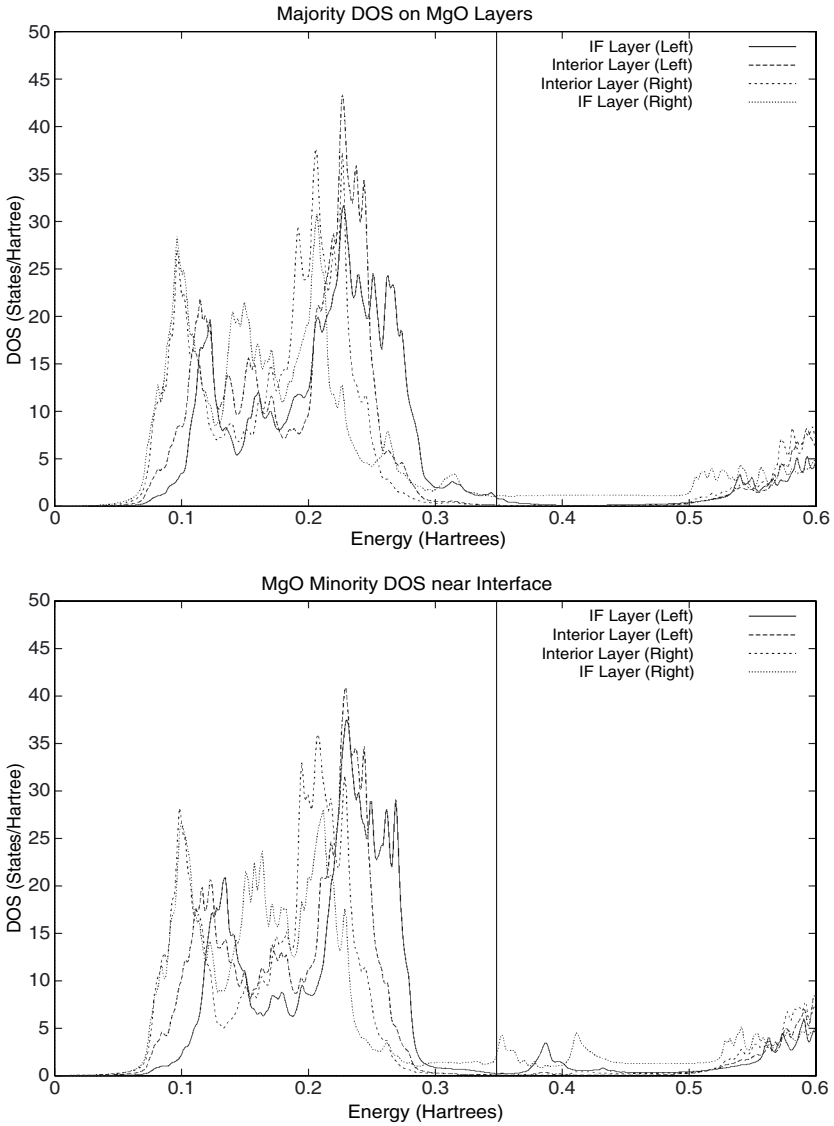

Figure 14. DOS for each of the atomic layers of MgO.

The scattering solution of Bloch electrons in the interface region described below follows [13]. It is similar to the techniques developed by Stiles and Hamann [28, 29] to calculate the transmission of Bloch waves through interfaces, that used a variational procedure of Wachutka and Bross [44, 45] to join wavefunctions on opposite sides of an interface.

Because we only consider $\mathbf{k}_\parallel$ conserving scattering at the interface, we will omit the label $\mathbf{k}_\parallel$ for Bloch states in all subsequent equations. The Bloch states for the bulk material that makes up the leads are labelled by k_z and the sign of the group velocity, v_z. Between each layer the Bloch wave is expanded in terms of plane waves.

$$\phi_{k_z^\pm} = \sum_{\mathbf{g}} c^+_{k_z^\pm \mathbf{g}} e^{i\mathbf{K}^+_{\mathbf{g}}\cdot\mathbf{r}} + \sum_{\mathbf{g}} c^-_{k_z^\pm \mathbf{g}} e^{i\mathbf{K}^-_{\mathbf{g}}\cdot\mathbf{r}}, \tag{26}$$

where the sum runs over the N_g reciprocal lattice vectors that are needed to accurately represent the wavefunction. The wavevectors $\mathbf{K}_{\mathbf{g}}^{\pm}$, in the plane waves $\exp(\mathrm{i}\mathbf{K}_{\mathbf{g}}^{\pm}\cdot\mathbf{r})$, are given by

$$\mathbf{K}_{\mathbf{g}}^{\pm} = \left\{\mathbf{k}_{\parallel}+\mathbf{g}, \pm\sqrt{\frac{2m}{\hbar^2}E-(\mathbf{k}_{\parallel}+\mathbf{g})^2}\right\}, \tag{27}$$

where the vectors $\mathbf{g}$ are two-dimensional reciprocal lattice vectors. Conversely, a plane wave can be expanded in terms of the Bloch wavefunctions, $\phi_{k_z}(\mathbf{r})$,

$$\mathrm{e}^{\mathrm{i}\mathbf{K}_{\mathbf{g},\mathbf{r}}^{\pm}} = \sum_{k_z^+}\mu_{\mathbf{g}k_z^+}^{\pm}\phi_{k_z^+}(\mathbf{r}) + \sum_{k_z^-}\mu_{\mathbf{g}k_z^-}^{\pm}\phi_{k_z^-}(\mathbf{r}). \tag{28}$$

The expansion coefficients, μ, can be found from the inverse of the matrix of eigenvector coefficients c.

We can expand the total wavefunction on the left-hand side of the barrier due to an incident wave plane wave with wavevector $\mathbf{K}_{\mathbf{g}^+}$ in terms of Bloch waves and obtain

$$\psi_{\mathbf{g}}^{+} = \sum_{k_z^+}A_{\mathbf{g}^+k_z^+}^{\mathrm{L}}\phi_{k_z^+}^{\mathrm{L}}(\mathbf{r}) + \sum_{k_z^-}A_{\mathbf{g}^+k_z^-}^{\mathrm{L}}\phi_{k_z^-}^{\mathrm{L}}(\mathbf{r}) = \mathrm{e}^{\mathrm{i}\mathbf{K}_{\mathbf{g}}^{+}\cdot\mathbf{r}} + \sum_{\mathbf{g}'}t_{\mathbf{g}\mathbf{g}'}^{+-}\mathrm{e}^{\mathrm{i}\mathbf{K}_{\mathbf{g}'}^{-}\cdot\mathbf{r}}, \tag{29}$$

where

$$A_{\mathbf{g}^+k_z^{\pm}}^{\mathrm{L}} = \mu_{\mathbf{g}k_z^{\pm}}^{\mathrm{L}+} + \sum_{\mathbf{g}'}t_{\mathbf{g}\mathbf{g}'}^{+-}\mu_{\mathbf{g}'k_z^{\pm}}^{\mathrm{L}-}. \tag{30}$$

The same wavefunction on the right-hand side of the barrier is

$$\psi_{\mathbf{g}}^{+} = \sum_{k_z^+}A_{\mathbf{g}^+k_z^+}^{\mathrm{R}}\phi_{k_z^+}^{\mathrm{R}}(\mathbf{r}) + \sum_{k_z^-}A_{\mathbf{g}^+k_z^-}^{\mathrm{R}}\phi_{k_z^-}^{\mathrm{R}}(\mathbf{r}) = \sum_{\mathbf{g}'}t_{\mathbf{g}\mathbf{g}'}^{++}\mathrm{e}^{\mathrm{i}\mathbf{K}_{\mathbf{g}'}^{+}\cdot\mathbf{r}}, \tag{31}$$

with

$$A_{\mathbf{g}^+k_z^{\pm}}^{\mathrm{R}} = \sum_{\mathbf{g}'}t_{\mathbf{g}\mathbf{g}'}^{++}\mu_{\mathbf{g}'k_z^{\pm}}^{\mathrm{R}+}. \tag{32}$$

The scattering matrices, $t_{\mathbf{g}\mathbf{g}'}^{++}$ and $t_{\mathbf{g}\mathbf{g}'}^{+-}$, are the transmission and reflection amplitudes of plane waves onto the slab of interface layers, as described in [27]. The superscripts $\pm$ refer to the direction of travel of incident and outgoing plane waves respectively.

A similar calculation can be performed for an incident plane wave from the right. The formulae for the coefficients $A_{\mathbf{g}^-k_z^{\pm}}^{\mathrm{R}}$ $A_{\mathbf{g}^-k_z^{\pm}}^{\mathrm{L}}$ can be simply obtained by swapping the superscripts L and R and '+' and '−' on the plane wave labels. We have used superscripts L and R to allow for the possibility that the leads on the left and on the right may have different Bloch states. This superscript is also used to imply appropriate values of $k_z^{\pm}$, since these too may be different in each lead.

If we now view the whole process as scattering of the Bloch waves, then the amplitude of the outgoing Bloch wave on the left-hand side of the barrier, $A_{k_z^-}^{\mathrm{L}}$, will be the sum of the transmitted Bloch waves from the right, $A_{k_z^-}^{\mathrm{R}}T^{--}$, and the reflected part of Bloch waves incident from the left, $A_{k_z^+}^{\mathrm{L}}T^{+-}$. Thus $A_{\mathbf{g}^{\pm}k_z^-}^{\mathrm{L}}$ is given by

$$A_{\mathbf{g}^{\pm}k_z^-}^{\mathrm{L}} = \sum_{k_z'^+}A_{\mathbf{g}^{\pm}k_z'^+}^{\mathrm{L}}T_{k_z'^+k_z^-}^{+-} + \sum_{k_z'^-}A_{\mathbf{g}^{\pm}k_z'^-}^{\mathrm{R}}T_{k_z'^-k_z^-}^{--}, \tag{33}$$

where $T_{k_z'^+k_z^-}^{+-}$ and $T_{k_z'^-k_z^-}^{--}$ are the reflection coefficients for Bloch waves incident from the left, and the transmission coefficients for Bloch waves incident from the right respectively. The

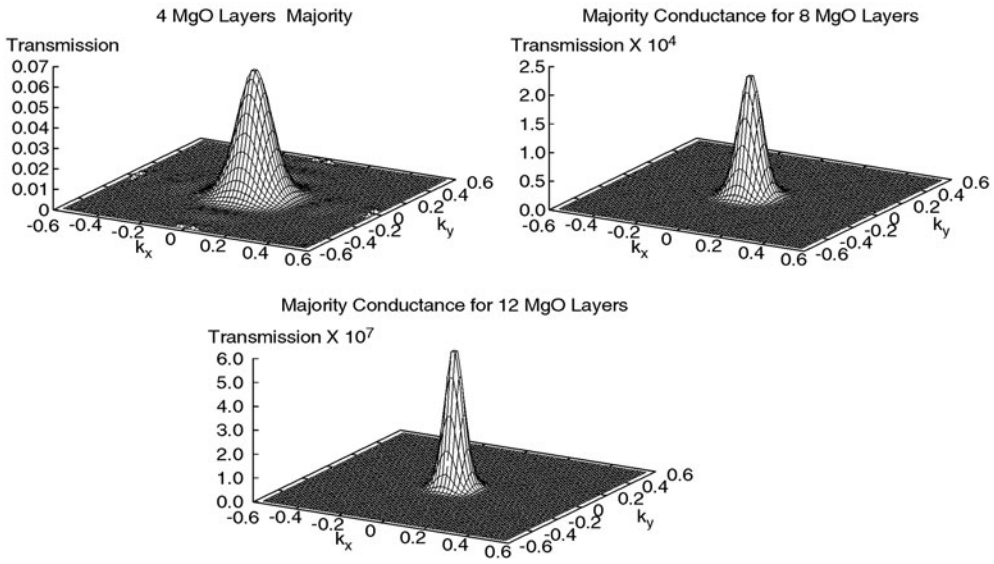

Figure 15. Majority conductance for four, eight, and 12 layers of MgO. Units for k_x and k_y are inverse bohr radii.

right travelling Bloch waves on the right side of the barrier are also a sum of reflected and transmitted Bloch waves:

$$A^{\mathrm{R}}_{\mathbf{g}^{\pm}k_z^{+}} = \sum_{k_z'^{+}} A^{\mathrm{L}}_{\mathbf{g}^{\pm}k_z'^{+}} T^{++}_{k_z'^{+}k_z^{+}} + \sum_{k_z'^{-}} A^{\mathrm{R}}_{\mathbf{g}^{\pm}k_z'^{-}} T^{-+}_{k_z'^{-}k_z^{+}}. \tag{34}$$

$T^{++}_{k_z'^{+}k_z^{+}}$ and $T^{-+}_{k_z'^{-}k_z^{+}}$ are the transmission coefficients for Bloch waves incident from the left-hand side of the barrier, and reflection coefficients for Bloch waves incident from the right-hand side of the barrier.

The four equations represented by (equations (33) and (34)) can be combined into a matrix form,

$$\begin{pmatrix} A^{\mathrm{L}}_{\mathbf{g}^{+}k_z^{+}} & A^{\mathrm{R}}_{\mathbf{g}^{+}k_z^{-}} \\ A^{\mathrm{L}}_{\mathbf{g}^{-}k_z^{+}} & A^{\mathrm{R}}_{\mathbf{g}^{-}k_z^{-}} \end{pmatrix} S = \begin{pmatrix} A^{\mathrm{R}}_{\mathbf{g}^{+}k_z^{+}} & A^{\mathrm{L}}_{\mathbf{g}^{+}k_z^{-}} \\ A^{\mathrm{R}}_{\mathbf{g}^{-}k_z^{+}} & A^{\mathrm{L}}_{\mathbf{g}^{-}k_z^{-}} \end{pmatrix}, \tag{35}$$

where the S matrix is defined as

$$S = \begin{pmatrix} T^{++} & T^{+-} \\ T^{-+} & T^{--} \end{pmatrix}, \tag{36}$$

which can then be solved for T^{++}, T^{+-}, T^{-+}, and T^{--} in terms of the coefficients $A^{\mathrm{L,R}}_{\mathbf{g}^{\pm}k_z^{\pm}}$. An S matrix formed in the subspace of travelling Bloch waves, i.e. those that have a real value of k_z, is needed to evaluate the Landauer–Büttiker conductance. This formalism is not equivalent to a simple unitary transformation of the S matrix in a plane wave basis since each Bloch state contains waves travelling in both senses, or, equivalently a single plane wave is composed of Bloch states travelling in both senses.

The S matrix of equation (35) has dimensions $2N_g \times 2N_g$. The submatrix of S formed on the subspace of travelling Bloch states is unitary provided those Bloch states carry unit flux, i.e.

$$S_{\mathrm{travelling}} S^{\dagger}_{\mathrm{travelling}} = I. \tag{37}$$

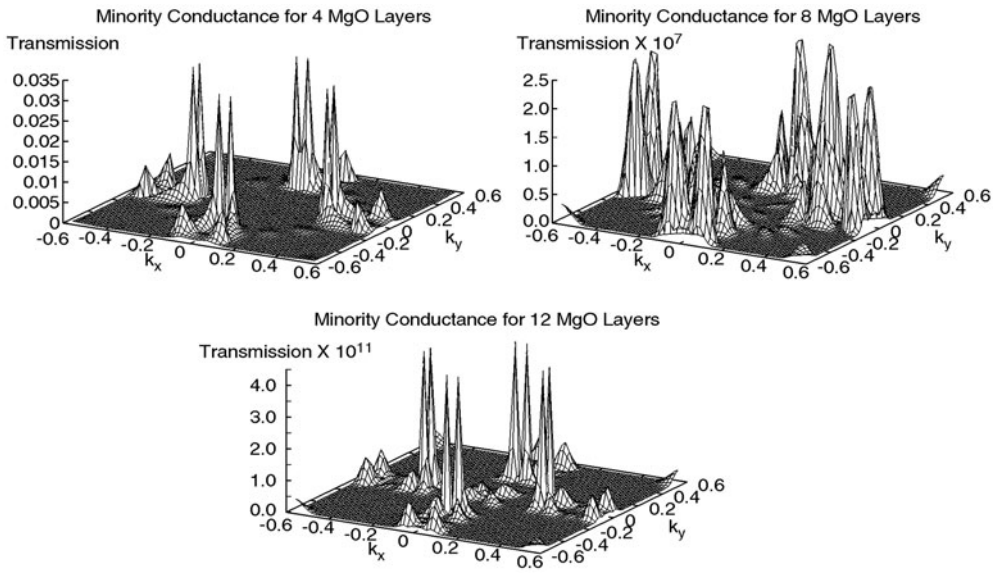

Figure 16. Minority conductance for four, eight, and 12 layers of MgO.

In computing the flux of each Bloch state, the plane wave basis set is used, and care must be taken to count correctly the contribution from both travelling and evanescent plane waves, since the expansion coefficients of the Bloch states are in general complex.

5. Tunnelling conductance at zero bias

The tunnelling conductances at zero bias have been calculated for a number of spin tunnelling junctions [13–18]. Although the absolute conductance depends on a number of factors, including the thickness of the barrier layer, the width of the barrier layer bandgap, and the geometry of the interfaces, the qualitative features of these systems are very similar. These features are that, for parallel alignment of the moments, the tunnelling conductance is typically dominated by the majority spin channel contribution which in turn is dominated by the contribution from $\mathbf{k}_\parallel = 0$; the minority spin channel conductance is dominated by tunnelling through interface resonance states, especially at small barrier thicknesses; TMR increases with the barrier layer thickness due to the diminishing influence of interface resonance states; and the decay rate of the tunnelling current in the barrier region is determined by the symmetry of the incident Bloch state and the complex bands (evanescent states) in the barrier. In this section we summarize these results using Fe|MgO|Fe and Fe|FeO|MgO|Fe as examples.

5.1. $\mathbf{k}_\parallel$*-resolved tunnelling current*

The calculated transmission probability as a function of $\mathbf{k}_\parallel$ for the majority spin channel is shown in figure 15 for four, eight, and 12 layers of MgO. Because of the two-dimensional periodicity, the crystal momentum parallel to the layers is conserved. For the majority channel, the conductance has a rather broad peak centred at $\mathbf{k}_\parallel = 0$. A somewhat similar peak is predicted for the tunnelling of free electrons through a simple square barrier [3]. The conductance observed here, however, differs significantly as is shown in figure 24 which shows

the transmission probability as a function of k_x for $k_y = 0$. The oscillations in transmission as a function of $\mathbf{k}_\parallel$ will be discussed later.

The tunnelling currents as a function of $\mathbf{k}_\parallel$ vary considerably with spin channel and moment alignment. For all thicknesses the majority spin current is peaked near the centre of the two-dimensional zone, while for thin barrier layers the minority spin current has peaks that seem to form part of a circle centred at the origin of the zone. This structure corresponds precisely to the localized resonance states seen at the interface in the minority spin channel. As the barrier layer becomes thicker, the currents at larger values of $\mathbf{k}_\parallel$ are suppressed and the current near $\mathbf{k}_\parallel = 0$ becomes relatively larger, but the point $\mathbf{k}_\parallel = 0$ remains a local minimum. The localized states which dominate the conductance in the minority channel at small thicknesses do not contribute as the barrier layer thickness is increased. The current for the anti-aligned case has features of both the majority and minority currents for the aligned case.

One important feature that is clear from comparing the three panels of figure 15 is the increasing concentration of the transmission in the region near $k_\parallel = 0$ as the insulating barrier layer is made thicker. This general feature would be expected from the simple model of a free electron incident on a square barrier of height V_B and thickness d for which the transmission probability contains a factor $\exp(-2d\kappa)$ where $\kappa^2 = (2m/\hbar^2)(V_B - E_F) + k_\parallel^2$. In real systems, the variation of the transmission is much more complicated as we shall discuss below. However, the strong concentration of majority transmission near $k_\parallel = 0$ and the fact that this region of the two-dimensional zone dominates the transmission for simple model barriers indicates that it is important to understand the tunnelling in detail for $k_\parallel = 0$.

Although the $\mathbf{k}_\parallel$ dependence of the majority channel conductance has at least superficial similarity to that of free electrons incident on a simple barrier, the minority channel conductance (figure 16) is completely different. The complicated, sharply peaked structure arises from the interplay of interfacial resonance states, the $\mathbf{k}_\parallel$ dependence of the wavefunction decay in the MgO (including interference effects), and the symmetry of the minority Fe Bloch states relative to that of the complex energy bands of MgO.

The transmission as a function of $\mathbf{k}_\parallel$ for anti-parallel alignment of the moments (figure 17) shows a combination of the features observed in the majority and minority channels. For thinner layers, the highest transmission is near the line $k_y = 0$ in the two-dimensional zone where there is an interfacial resonance state. As the layers become thicker, the highest transmission occurs closer to the origin of the two-dimensional zone due to the slow decay in the MgO of states derived from the Fe majority Δ_1 band.

5.2. Thickness dependence of conductance and magnetoconductance

The tunnelling conductance was calculated for the Fe|ZnSe|Fe sandwich composed of (100) planes as a function of the thickness of the ZnSe interlayer for majority and minority channels and for parallel and anti-parallel alignment of the moments in the two Fe layers [13]. The conductance is calculated from equation (9) by summing the transmission probability over the two-dimensional zone. The results, which are plotted in figure 18, show that the conductance is approximately an exponential function, $e^{-d/\ell}$, of the barrier thickness, d, with a length of decay, ℓ, that varies from approximately 4.6 Å for the majority electrons to approximately 3.7 Å for the minority electrons. The decay length for the majority electrons, can be estimated in terms of the conduction band minimum, E_c, the valence band maximum, E_v, and the effective mass, m^*, as

$$\kappa_0 = \frac{1}{2\ell} = \sqrt{\frac{2m^*}{\hbar^2}\frac{(E - E_v)(E_c - E)}{(E_c - E_v)}} \tag{38}$$

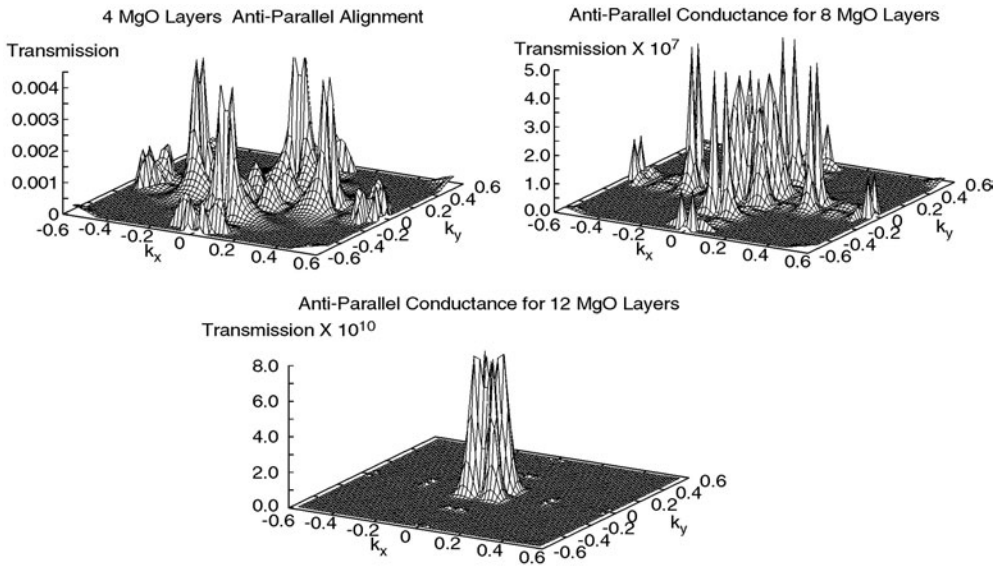

Figure 17. Conductance for anti-parallel alignment of the moments in the electrodes.

which is consistent with the estimate from the free electron model using the effective mass at the bottom of the conduction band of ZnSe. The thickness dependences of the majority channel conductance, of the minority channel conductance, and of the tunnelling conductance for either spin channel for the case of anti-parallel alignment are significantly different. The decay rates of the parallel alignment minority spin channel and the anti-parallel alignment are not uniform, and they are much closer to each other at thin barrier thicknesses. This is due to the conductance from the interfacial resonance states which is particularly important for very thin barriers. The more rapid decrease in the minority and anti-parallel conductance compared to the majority leads to a tunnelling conductance at large thicknesses that is dominated by the majority electrons. This yields a magnetoresistance ratio that approaches unity as shown in figure 19. This behaviour is quite different from that observed in calculations that were performed in which the barrier was a constant potential [24].

A similar plot of conductance as a function of thickness for the Fe|MgO|Fe sandwich is shown in figure 20. In this case, for all thicknesses, the majority conductance overwhelms the minority or the anti-parallel. Again, the magnetoconductance (not plotted here) should increase with thickness, with the conductance becoming dominated by the majority channel.

6. Role of electronic structure in tunnelling

First-principles calculations allow one to analyse in detail the effects of the electronic structure on tunnelling conductance and TMR. Although it is widely believed that the effective barrier height determines the decay rate of the tunnelling electrons, actual calculations show that this picture misses a large part of the physics. In particular, the lateral symmetry of the Bloch wavefunction plays a critical role in determining which complex band in the barrier matches to an incident Bloch wave. These complex bands in turn determine the decay rate in the barrier. Other factors that are important in determining tunnelling probability include the interface resonance states and the chemical bond effect. In this section we summarize these results.

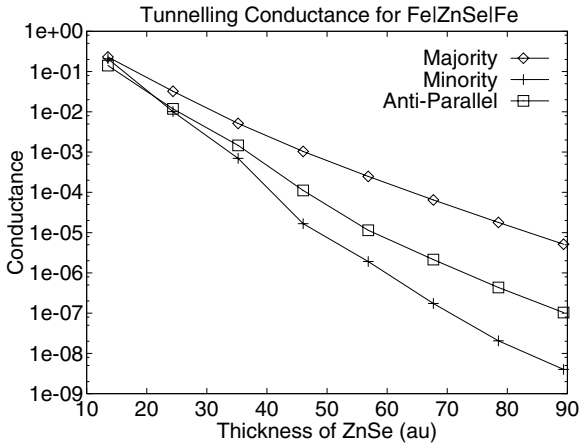

Figure 18. Tunnelling conductance as a function of the thickness of the barrier layer. The conductance is in units of e^2/h per two-dimensional unit cell.

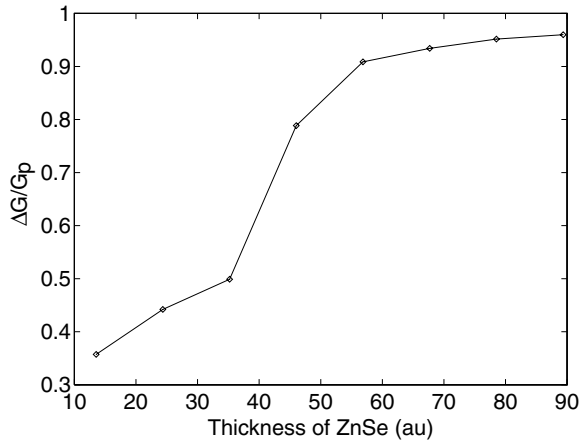

Figure 19. Magnetoresistance as a function of ZnSe thickness for an Fe|ZnSe|Fe sandwich. Here the ratio $\Delta G/G_{\mathrm{p}}$ is used instead of the common $\Delta G/G_{\mathrm{ap}}$ to highlight the approach of the ratio to unity for large insulator layer thickness.

6.1. Effect of symmetry at $k_{\parallel} = 0$

The differences in the barrier thickness dependence of the conductance for majority and minority electrons as well that for the antiparallel magnetic alignment, as shown in figures 19 and 20, are due to the different symmetry of the Bloch states at the Fermi energy. The decays of the various Fe(100) Bloch states into the barrier are quite similar for Fe|ZnSe|Fe, figure 21, and Fe|MgO|Fe, figure 22. Similar to the discussion of tunnelling through a vacuum barrier in section 2.3, there are three decay rates associated with different angular momentum characters of the four Bloch states for each spin channel. The rate of decay is slowest for bands with s character and most rapid for those with only d character. In addition to the different decay rates, the ease of injection and extraction is also band dependent. Because of the s character of the Δ_1 band in the majority spin channel, it couples efficiently with a decaying sp state in the

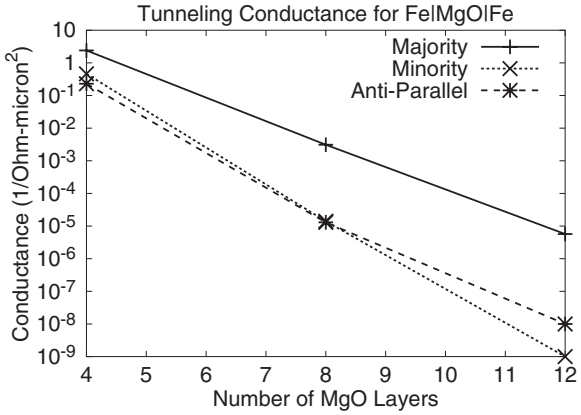

Figure 20. Conductance as a function of the number of MgO layers.

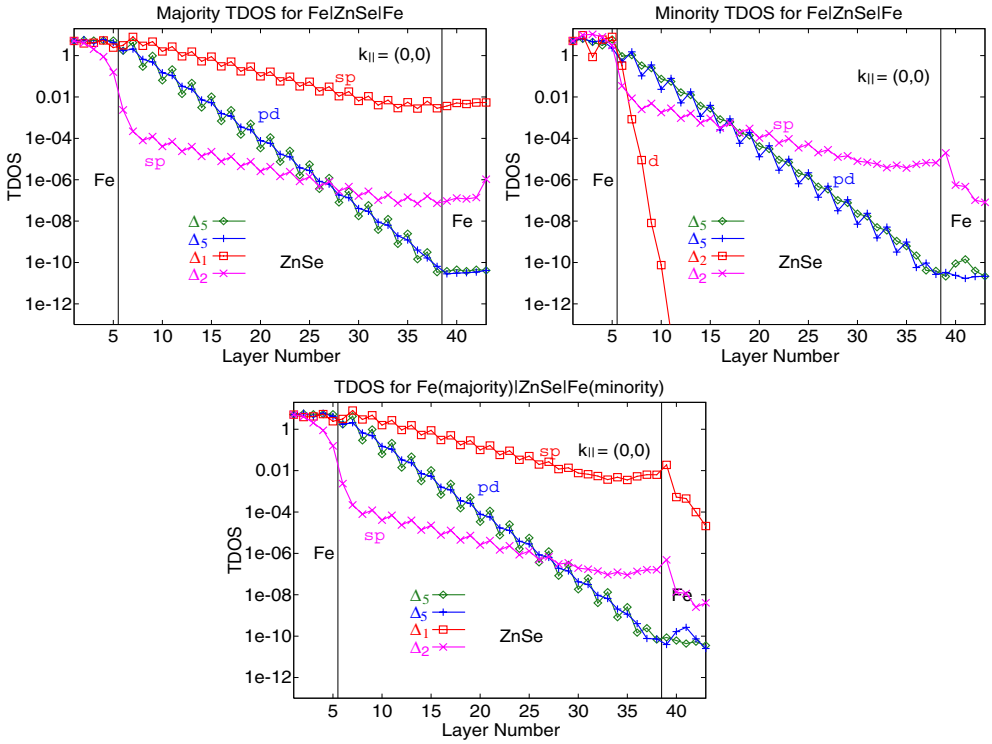

Figure 21. Tunnelling DOS for each of the Bloch states at $k_{||} = 0$ for an Fe|ZnSe|Fe tunnelling junction. The top two panels are for parallel alignment of the Fe moments; the bottom panel is for anti-parallel alignment of the Fe moments, where the left-hand side of the junction is spin up, while the right-hand side is spin down.

barrier, and thus this band dominates the conductance. The $\Delta_{2'}$ bands for both spins are pure d-bands in the bulk, so they cannot couple with the sp state in the barrier layer. The small sp component in the $\Delta_{2'}$ bands seen in figure 21 for Fe|ZnSe|Fe and absent in the similar plots in both figure 22 for Fe|MgO|Fe and figure 5 for Fe|vacuum|Fe, is probably due to the lack

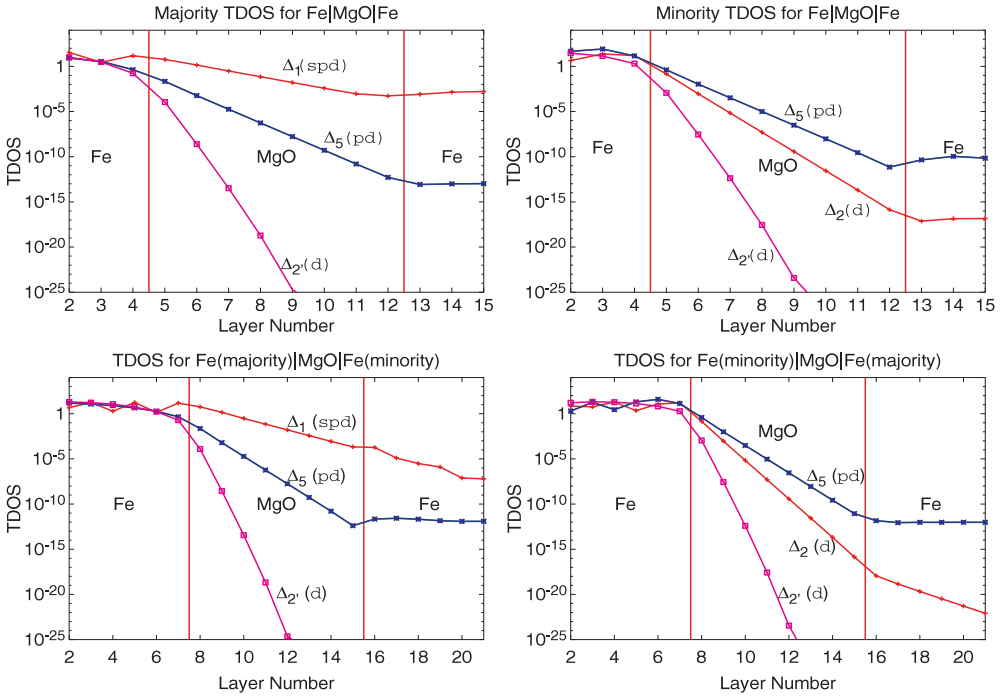

Figure 22. Tunnelling DOS for $k_{\|} = 0$ for Fe(100)|8MgO|Fe(100). The four panels show the TDOS for majority (upper left), minority (upper right), and anti-parallel alignment of the moments in the two electrodes (lower panels). Additional Fe layers are included in the lower panels to show the TDOS variation in the Fe. Each curve is labelled by the symmetry of the incident Bloch state in the left Fe electrode.

of convergence in the plane wave basis for the Fe|ZnSe|Fe calculation, which needed a larger two-dimensional unit cell than the other calculations, and was at the limit of the numerical capability of the layer-KKR code. Therefore we believe that the actual decay rate of the $\Delta_{2'}$ bands in figure 21 should be much faster, although this should have little effect on the total tunnelling conductance and the TMR. The doubly degenerate Δ_5 band couples to a pd decaying state in the barrier and as a consequence decays more rapidly. Similar arguments apply to the minority spin channel, and the much smaller tunnelling conductance is a direct result of the absence of the Δ_1 band at the Fermi energy.

The absence of the Δ_1 band in the minority spin channel is also the reason that the maximum conductance for anti-parallel alignment does not occur exactly at $k_{\|} = 0$, as illustrated from the bottom panels of figures 21 and 22 which show the TDOS for anti-parallel alignment at $k_{\|} = 0$. On the left-hand side of the barrier the majority band Δ_1 electrons readily enter the barrier where they decay slowly with distance as discussed in section 6.1. On the right-hand side of the barrier, however, these states continue to decay within the minority spin channel of bulk Fe, resulting in the total reflection of the Δ_1 Bloch state. Consequently the tunnelling conductance is dominated by the Δ_5 electrons which decay relatively rapidly in the barrier, but are able to enter the minority spin channel of bulk Fe relatively easily because there are states to receive them. The $\Delta_{2'}$ electrons decay extremely rapidly as discussed for the cases of majority and minority conductance. A similar total reflection also occurs to the minority Δ_2 state incident from the left, as shown in the lower right panel of figure 22.

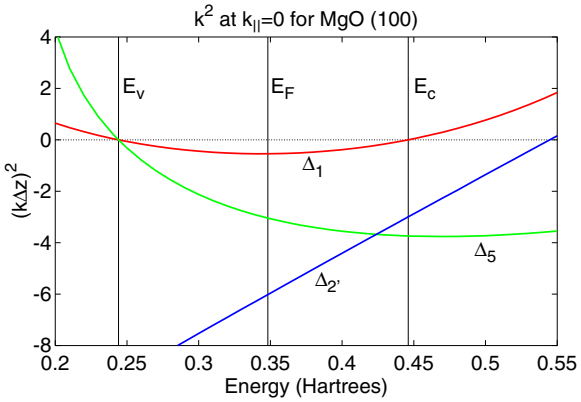

Figure 23. Dispersion $k^2(E)$ for MgO in the vicinity of the gap along Δ (100). Negative values of k^2 determine the exponential decay rates for various Bloch states. E_v is the top of the valence band. E_c is the bottom of the conduction band.

6.2. Decay rates determined by complex bands in barrier

One convenient way to understand the relationship of the decay rates in the barrier layer and the electronic structure of the barrier, in place of the simplistic description of an 'effective barrier height', is to consider the complex bands within the bandgap of the barrier material [14, 33]. The complex bands for energies in the vicinity of the gap for bulk MgO are plotted in figure 23. In this figure, we plot $k^2(E)\Delta z$ along the [100] (Δ) direction for the three symmetries (Δ_1, Δ_5, and $\Delta_{2'}$), where Δz is the interplanar spacing for MgO(001) and $k(E)$ is in the (001) direction. For each symmetry only the complex band with the smallest values of $|k^2|$ in the vicinity of the Fermi energy is plotted. The nearest complex band with symmetry Δ_2 would cross the Fermi energy with a value of $-(k\Delta z)^2$ of approximately 31.5. The energy range for which all values of k^2 are less than zero is the energy gap. The remaining symmetry in the (001) direction, $\Delta_{1'}$, which is not represented in Fe or MgO near the Fermi energy, has a minimum angular momentum of $\ell = 4$ and presumably only yields a real band at very high energy. It would correspond to a state that decays extremely rapidly.

The slowest decay rate is for states with Δ_1 symmetry which are predicted to decay at the rate $\exp(-2\kappa\Delta z)$ where $\kappa\Delta z = \sqrt{-(k_{\Delta_1}\Delta z)^2} \approx 1.47$. Band states in MgO with Δ_1 symmetry occur at both the bottom and the top of the energy gap. The next slowest decay rate is for states with Δ_5 symmetry. There is a high mass Δ_5 band at the top of the valence band. The $\Delta_{2'}$ state becomes a band state about 2.7 eV above the bottom of the conduction band. However, it becomes real at the X point ($k\Delta z = \pi$); thus π has been subtracted from $k\Delta z$ for the $\Delta_{2'}$ state for the purposes of plotting the decay rates in figure 23.

Majority Bloch states with Δ_1 symmetry in the Fe electrodes decay as evanescent states with Δ_1 symmetry in MgO. Similarly, Δ_5 Bloch states which occur for both majority and minority Fe(100) decay as evanescent states with the same symmetry in the MgO. The $\Delta_{2'}$ Bloch states which have xy symmetry and which occur in both the majority and minority Fe(100) channels, however, decay as Δ_2 states in the MgO. Similarly, the $\Delta_{2'}$ states decay as Δ_2 states in the MgO. The reason for this is not a mysterious change in the symmetry of the wavefunctions, but is due to the fact that the MgO cubic cell is rotated by $\pi/4$ with respect to that of the Fe thus states with $x'y'$ symmetry in Fe have $x^2 - y^2$ symmetry in MgO where (x, y) and (x', y') are related by a $\pi/4$ rotation. The results of these symmetries and the predictions of the decay rates from the complex bands are in perfect agreement with figure 22.

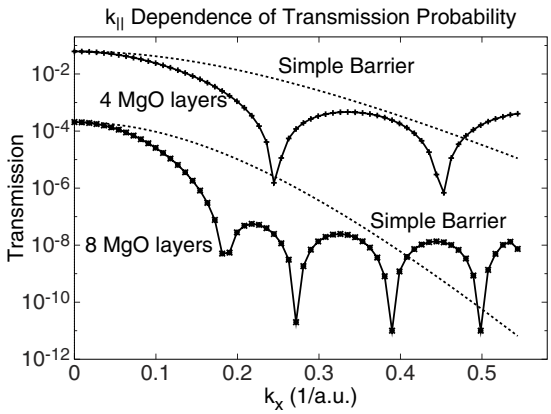

Figure 24. Majority transmission probability as a function of $k_\parallel$ for $k_y = 0$ for four and eight layers of MgO. The curves end before the zone boundary is reached because there are no states for $k_x > 0.55$ au^{-1}. Smooth curves show the expected behaviour of the transmission probability from equation (39).

6.3. Interference of tunnelling states

The first-principles results summarized in the preceding subsections showed that states with different symmetry decay at different rates as they tunnel through the barrier. Another important result from first-principles calculations that is contrary to the simple barrier model is the variation of the tunnelling current with $k_\parallel$. Figure 15 gives an overall representation of the majority tunnelling current throughout the two-dimensional Brillouin zone. However, additional detail and structure can be seen if the transmission is presented on a logarithmic scale as is shown in figure 24. The smooth curves in the figure labelled 'Simple Barrier' are functions $\exp(-2d\kappa)$ where d is the thickness of the barrier and κ is given by [3]

$$\kappa^2 = \frac{2m^*}{\hbar^2}(V_B - E) + k_\parallel^2 = \kappa_0^2 + k_\parallel^2. \tag{39}$$

Evidently the simple barrier model represented by this equation cannot describe the actual dependence of $\mathbf{k}_\parallel$. In particular, the initial decrease of transmission is much faster than that given by equation (39), and it also appears that the $k_\parallel$ dependence is oscillatory, as if there were wave interference within the barrier!

It has recently been noted [18] that oscillations of the conductance in Fe|semiconductor|Fe sandwiches may arise from a quantum well resonance within the barrier layer *when transmission occurs through propagating states in the semiconductor*. This is a very well known result that is expected from simple models. Figure 15 shows, however, a much more surprising result. The analysis of [14] showed that the oscillations in the transmission that occur as a function of $k_\parallel$ result from the complex band structure of MgO in the energy gap. The complex values of k_z at the Fermi energy are plotted as a function of $k_\parallel$ in figure 25. The two states shown have the lowest value of the imaginary part of k_z and are therefore the most important for determining the transmission probability. The states are plotted as a function of $k_\parallel$ along $\bar{\Gamma}$ to $\bar{\mathrm{X}}$. The smooth curves which provide a good fit to the complex values of k_z are the given by the formula

$$\theta_z - \mathrm{i}\bar{\theta}_0 = \frac{\theta_x}{\sqrt{2}} \pm a\sqrt{(\theta_x - \eta)(\theta_x + \xi)}, \tag{40}$$

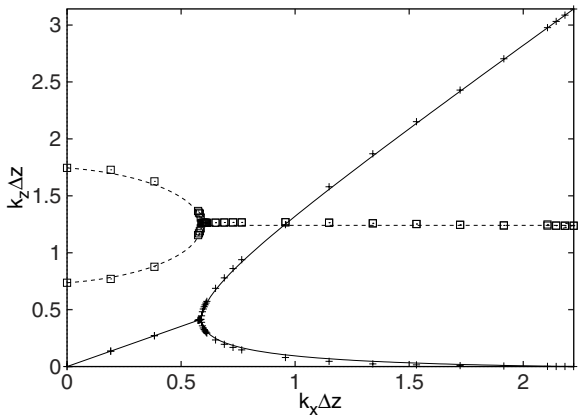

Figure 25. Real and imaginary parts of k_z plotted as a function of k_x for MgO. The two values of k_z with the smallest imaginary parts are shown. Plus symbols (squares) denote values of the real (imaginary) part of k_z calculated with the LKKR code. The solid and dotted curves are the real and imaginary parts, respectively, of the fit to complex k_z described in the text.

where $\theta_z = k_z\Delta z$ and $\theta_x = k_x\Delta z$. The constants, $\bar{\theta}_0$, a, η, and ξ are determined in the following way: $\bar{\theta}_0 = (\theta_z^{\Delta_1} + \theta_z^{\Delta_5})$ is the average of the two imaginary roots for $\theta_x = 0$. η is the value of θ_x for which the curves in figure 25 bifurcate. a and ξ are determined by the difference of the two imaginary roots at $\theta_x = 0$ and by the requirement that $\theta_z = \pi$ or 0 at $\theta_x = \pi/\sqrt{2}$.

The behaviour of the complex values of k_z shown in figure 25 explains the interesting interference effects shown in figure 24. For $k_x\Delta z$ less than 0.59, the point of bifurcation, the transmission is predicted to decay as $|\psi|^2$ where $\psi = \exp(\mathrm{i}k_1 d) + \exp(\mathrm{i}k_2 d)$ with k_1 and k_2 representing the two complex k_x-dependent values of k_z. Thus for $k_x\Delta z < 0.59$,

$$|\psi|^2 = \mathrm{e}^{-2\kappa_1 d} + \mathrm{e}^{-2\kappa_2 d} + 2\mathrm{e}^{-\kappa_1 d - \kappa_2 d} \tag{41}$$

where $\kappa_{1(2)} = \mathrm{Im}[k_{1(2)}(k_x)]$, and the transmission decreases much faster with $k_\parallel$ than would be expected from equation (39). On the other hand, for $k_x\Delta z > 0.59$, the imaginary parts of k_1 and k_2 are equal so that

$$|\psi|^2 = 2\mathrm{e}^{-2\kappa(k_x)d}\{1 + \cos[k_1^{\mathrm{r}}(k_x) - k_2^{\mathrm{r}}(k_x)]d\} \tag{42}$$

where k_1^{r} and k_2^{r} are the real parts of the two values of k_z. Thus the transmission is a damped oscillatory function of thickness and is a purely oscillatory function of k_x since κ is essentially independent of k_x for $k_x\Delta z > 0.59$.

The interference effect arising from equation (40) can be understood heuristically from the dispersion relation in the vicinity of the gap described within a tight binding model, expressed as a polynomial in $\cos(\theta_z)$ with real coefficients that depend on θ_x. The roots of this polynomial must be either real or they must occur as pairs that are complex conjugates. If the roots with the smallest imaginary part are complex conjugates, r, r^* then the values of θ_z can be found from

$$z^2 - 2rz + 1 = 0 \qquad z^2 - 2r^*z + 1 = 0 \tag{43}$$

where $z = \mathrm{e}^{\theta_z}$. Each of these equations has two roots, $z_1^{\pm} = r \pm \sqrt{r^2 - 1}$, $z_2^{\pm} = r^* \pm \sqrt{(r^*)^2 - 1}$. Because $z_1^+ z_1^- = z_2^+ z_2^- = 1$, we know that only two of these roots will represent decaying waves. Thus if $|z_1^+| < 1$, it follows that the two decaying roots, z_1^+ and z_2^+, have equal modulus, $|z_1^+| = |z_2^+|$. Thus the imaginary parts of θ_z for these two solutions will

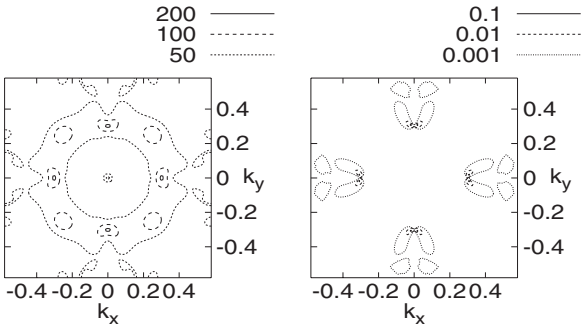

Figure 26. Minority DOS (states/hartree) on the interfacial Fe layer (left panel); transmission in the minority channel (right panel). Units of k_x and k_y are inverse Bohr radii.

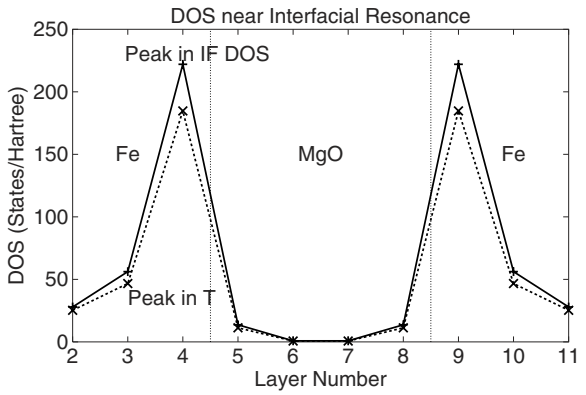

Figure 27. DOS on each layer for value of $\mathbf{k}_\parallel$ equal to that of the peak in minority interfacial DOS (higher values) and for the value of $\mathbf{k}_\parallel$ equal to the peak in the transmission (lower values).

be equal. This would lead to the observed interference effect. Note that this does not explain why the imaginary part of θ_z is almost independent of θ_x. Similar oscillatory behaviour for transmission through ZnSe tunnelling barriers was also seen so this may be a general feature of tunnelling through real materials.

6.4. Tunnelling through interface resonance states

The tunnelling conductance of the minority spin channel has a very different character from the majority spin channel. The sharp peaks in figure 16 are mainly due to interface resonance states [14, 16]. To see this, we first compare the $\mathbf{k}_\parallel$ resolved DOS on the interfacial iron layer with the transmission, shown as contour plots for the four-MgO-layer system in figure 26. The interfacial DOS is large in a ring surrounding the $\bar{\Gamma}$ point in the two-dimensional zone, with sharp peaks along the symmetry directions $k_x = 0$ and $k_y = 0$. These peaks correspond to the states strongly localized at the Fe–MgO interface. Figure 27 is a plot of the DOS on each layer at the peaks in the interfacial DOS ($k_x = 0.299, k_y = 0.000$) and in the transmission ($k_x = 0.308, k_y = 0.018$). The localization of the resonant states on the interface layer is evident for both values of $\mathbf{k}_\parallel$.

The presence of the interfacial resonance states leads to a huge wavefunction amplitude at the interface which, all other factors being equal, would in turn lead to a strong coupling to

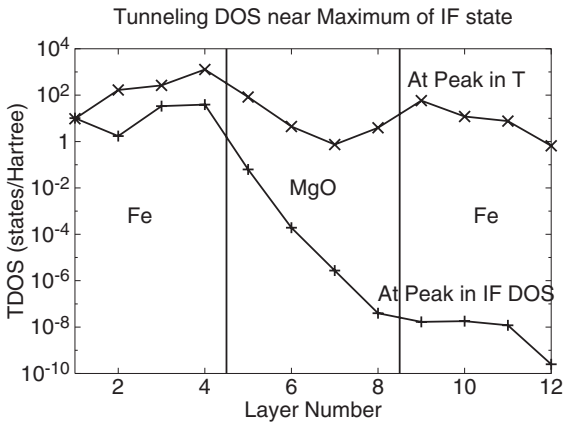

Figure 28. Tunnelling DOS at two neighbouring points in the two-dimensional zone. One point is at the peak in the transmission ($k_x = 0.308, k_y = 0.018$). The other is at the peak in the interfacial DOS ($k_x = 0.299, k_y = 0.000$).

the evanescent states in the barrier and a large transmission probability. However, this is only part of the story because the transmission is actually quite low for the value of $\mathbf{k}_\parallel$ for which the DOS of the interfacial resonance is highest. The decay rate in the barrier is also important, which for a given value of $\mathbf{k}_\parallel$ is determined by the wavefunction symmetry as we discussed in section 2.3. Figure 28 shows the TDOS both at the peak in the interfacial DOS and at the peak in the transmission. There is a large difference in the rate of decay of the TDOS in the two cases. Because the Bloch state at $k_x = 0.299, k_y = 0$ (the peak in the interfacial DOS) has no s character, it can only couple to an evanescent state in the MgO that decays rapidly. Very slightly out of the $k_y = 0$ plane, however, the wavefunction has significant s character and can couple to an evanescent state that decays slowly.

6.5. Chemical bond effect

Interface resonance states have a dramatic impact on the minority spin conductance but have very little influence on the majority spin conductance. Recently, we have discovered a different mechanism [42], a chemical bond effect in the Fe|FeO_x|MgO|Fe tunnel junction, that can change the majority spin conductance by more than an order of magnitude, while having minimal impact on the minority spin conductance. To investigate the role of oxygen in the FeO layer, which is often unavoidable during the growth of the film [40, 41], we used the coherent potential approximation [43] to study the TMR as a function of oxygen concentration in the FeO layer. The result plotted in figure 29 shows that, after initial small changes for low oxygen concentration, the ratio of parallel and anti-parallel conductances drops exponentially as the oxygen percentage increases above 50%. The first clue that this is a chemical bond effect is the change of the dipole moment on the Fe ASA sphere in the FeO layer as a function of oxygen content, plotted in the same figure. This moment drops from about 0.19 electrons × Bohr (au) at zero per cent oxygen to 0.05 electrons × au at 100% oxygen. For reference, the corresponding Fe dipole moment on a clean Fe surface is about 0.22 electrons× au. The dipole moment on the oxygen ASA sphere in the FeO layer stays in the range between 0.06 and 0.08 electrons× au as a function of oxygen concentration. [42] showed through the examination of the charge distribution at the Fermi energy and the net charge on the oxygen atoms that the Fe–O bonds remove a sheet of electrons from the interface region, which causes the reduction of the tunnelling conductance.

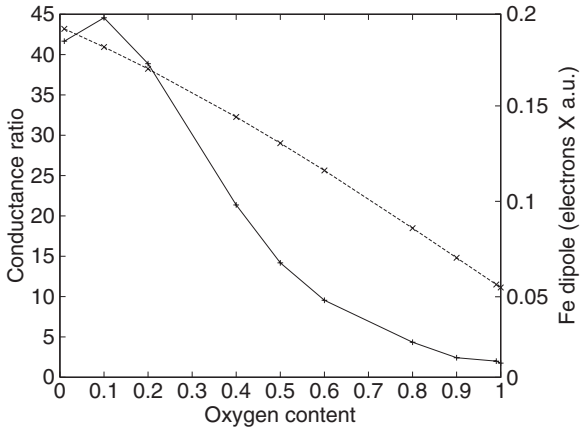

Figure 29. TMR as a function of oxygen composition on the interface FeO layer. The solid curve is the conductance ratio $\Delta G/G_{\rm ap}$; the dashed curve is the dipole moment.

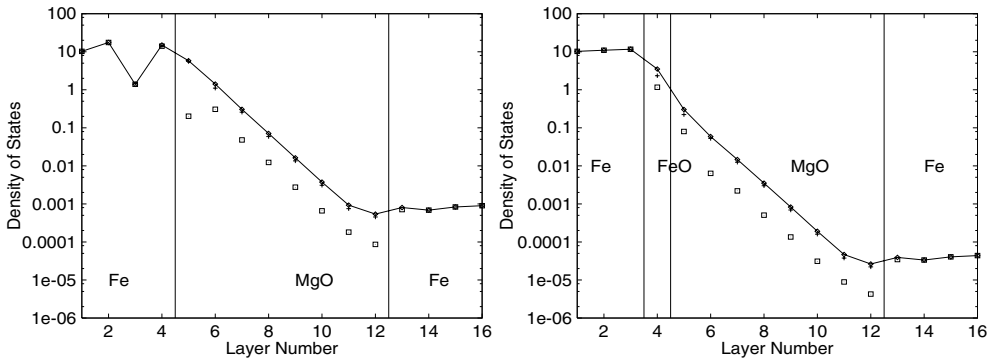

Figure 30. Tunnelling DOS for $k_{\|} = 0$ for Fe(100)|8MgO|Fe(100) and Fe(100)|FeO|8MgO|Fe(100). The diamonds connected with lines are the TDOS summed over each atomic layer. The crosses are the TDOS on the oxygen spheres. The squares are the TDOS on the Mg spheres in the MgO layer or on the Fe spheres in the Fe(100) layers or the FeO layer.

The TDOSs at $\mathbf{k}_{\|} = 0$, with and without the FeO layer, are compared in figure 30. The change in the TMR ratio is dominated by the change in the parallel majority spin conductance, which in turn is dominated by the contribution from $\mathbf{k}_{\|} = 0$ Bloch electrons. Comparing the TDOS in figure 30 for the Δ_1 state between the Fe|FeO|MgO|Fe stack and the Fe|MgO|Fe stack, we can see that the tunnelling state decay rate is about the same within the MgO layer, and the coupling between the tunnelling state in MgO and the outgoing Bloch state in the right-hand Fe lead is also about the same. The big difference that causes the more than one order of magnitude drop in the tunnelling conductance comes from the reduced coupling of the incident Bloch state from the left-hand Fe lead though the FeO layer into MgO.

We also plotted in figure 30 the TDOS on individual atomic spheres in these layers. It is obvious from the plot that on layers where oxygen atoms are present they dominate the TDOS. Consequently, most of the tunnelling current flows through the oxygen sites. However, the symmetry of the wavefunction on the oxygen site in the FeO layer is very different from that of the oxygen site in the MgO layer. This is evident from the different ratios between the partial DOS in s and p components. According to our calculation, the Δ_1 state in MgO has about

the same order of magnitude s and p components on the oxygen site, with the p component somewhat larger than s. On the FeO oxygen site, the p component is more than an order of magnitude larger than the s component. Thus, in order for the wavefunctions to match across the layers, a much smaller fraction can be transmitted through the FeO layer compared to when there is no FeO present.

The reduction of TMR when there is an FeO layer present is clearly due to the formation of intralayer Fe–O bonds. Without the FeO layer, a sheet of electron density similar to that on a clear iron surface exists between the interface iron atom and the first MgO layer and provides a path of low resistance for the tunnelling current. With the FeO layer, as a function of increasing oxygen concentration, the electron density becomes more and more concentrated within the FeO plane and confined within the Fe–O bond thus greatly reducing the tunnelling current through the iron atoms. At 100% oxygen the tunnelling current flows almost entirely through the oxygen atom. Due to the mismatch of the wavefunctions between the oxygen orbitals within the FeO layer and those within MgO, the tunnelling current for the parallel configuration is greatly reduced. The antiparallel current, dominated by the contribution from interface resonance states, is actually increased slightly by the oxidization of the interface iron layer. This is probably due to the rearrangement of the interface resonance states which coincidentally match much better for one of the (anti-aligned) spin channels. This leads to a much smaller TMR ratio.

In [35] the possible effect of chemical impurities on the interface was discussed based on a change of the interface magnetic moment caused by the introduction of impurities. It was argued that if the chemical bond effect reduced the magnetic moment on the interface, then a reduced spin polarization of the interfacial DOS would lead to a corresponding reduction in the spin polarization of the tunnelling current. Our calculation shows that if there is any connection between the magnetic moment and the spin polarization of the tunnelling current, such connection is not consistent with the above argument. In the case of Fe|FeO|MgO|Fe, the magnetic moment of the iron atom in the FeO layer is 3.33 μ_B, about 10% higher than the value of 2.97 μ_B at the interface of Fe|MgO.

7. Conclusions

A number of common themes have emerged from the first-principles studies of spin-dependent tunnelling junctions. We believe that the following results apply rather generally to tunnelling in epitaxial systems and to be contrary to the simple barrier model that is typically used to describe electron tunnelling.

(1) The symmetry of the Bloch states at the Fermi energy and their relationship to the symmetry of the slowly decaying evanescent states in the barrier layer are crucial to understanding tunnelling conductance. Note that for electrons with $k_{\|} = 0$, these states and their symmetries can be obtained from ordinary band structure calculations.
(2) There will typically be more than one evanescent state in the barrier layer at the Fermi energy. It is possible, even likely, that the tunnelling conductance will be affected by interference between these states. It is not yet clear to us whether this interesting prediction can be observed experimentally.
(3) Interfacial resonance states can, through their effect on the wavefunction matching at the interface, significantly enhance the tunnelling probability.

Results that are particular to tunnelling through epitaxial insulators on Fe(100) Include the following.

(1) Majority channel tunnelling is dominated by the transmission through a Δ_1 state at small values of transverse crystal momentum.
(2) Minority channel tunnelling is smaller and is strongly enhanced for values of $\mathbf{k}_\parallel$ near interfacial resonance states.
(3) TMR increases with thickness. Conclusions (2) and (3) are tempered by the caveat that the interfacial resonance states seem to be very sensitive to the details of the interface.
(4) The nature of the chemical bonding at the interface and its effect on the wavefunctions at the Fermi energy can greatly influence the tunnelling conductance and the TMR. A single atomic layer of FeO can cut the conductance by more than an order of magnitude through the formation of intralayer Fe–O bonds.

Insights that may be relevant to the more general problem of tunnelling through non-epitaxial barriers include the observation that the state with the slowest decay rate in the barrier is typically one with significant s or free electron character. Thus the reason that the tunnelling conductance has been shown to be dominated by majority electrons, in those cases where the spin dependence of the conductance could be determined by use of a superconducting electrode, may simply be that, for most of the magnetic transition metals and their alloys, the majority Fermi energy DOS has more free electron or s-like character than the minority, which is typically is predominantly d-like. The reason that the d electrons do not tunnel efficiently is that they have a much higher decay rate in the barrier because of their additional in-plane oscillations.

An additional general observation is that, all other parameters being equal, tunnelling rates are higher if there are similar or identical states on both sides of the barrier. Thus the tunnelling electrons need not only to get through the barrier, but there must be a state of the correct symmetry on the other side to accept them. The symmetry matching or mismatching of the wavefunctions on both interfaces should be an important consideration, especially in the case of a finite voltage bias which would tend to move similar states on both interfaces away in energy.

Acknowledgments

This research was supported by the Defense Advanced Projects Agency through ONR contract N00014-02-01-0590 and by the Office of Science of the USDOE. Oak Ridge National Laboratory is operated by UT-Battelle, LLC, for the US Department of Energy under contract DE-AC05-00OR22725. Work at the University of Alabama was supported in part by National Science Foundation MRSEC grant number DMR0213985. We thank our collaborators who have assisted in the modelling of TMR systems, especially Thomas Schulthess and James MacLaren. We also thank Dr K D Belaschenko for helpful discussions regarding TMR and the factorization of the tunnelling probability.

References

[1] Baibich M N, Broto J M, Fert A, Nguyen Van Dau F, Petroff F, Eitenne P, Creuzet G, Friederich A and Chazelas J 1988 *Phys. Rev. Lett.* **61** 2472
[2] Jin S, Tiefel T H, McCormack M, Fastnacht R A, Ramesh R and Chen L H 1994 *Science* **264** 5157
[3] Julliere M 1975 *Phys. Lett.* A **54** 225
[4] Tedrow P M and Meservey R 1971 *Phys. Rev. Lett.* **26** 192
Tedrow P M and Meservey R 1973 *Phys. Rev.* B **7** 318
[5] Slonczewski J C 1989 *Phys. Rev.* B **39** 6995

[6] Maekawa S and Gäfertm U 1982 *IEEE Trans. Magn.* **18** 707
[7] Suezawa Y and Gondo Y 1987 *Proc. Int. Symp. on Physics of Magnetic Materials, MAG-18 (Sendai)* p 303
[8] Miyazaki T and Tezuka N 1995 *J. Magn. Magn. Mater.* **151** 403
[9] Moodera J S, Kinder L R, Wong T M and Meservey R 1995 *Phys. Rev. Lett.* **74** 3273
[10] Tehrani S, Chen E, Durlan M, Deherrera M, Slaughter J M, Shi J and Kerszykowski G 1999 *J. Appl. Phys.* **85** 5822
[11] Parkin S S P, Roche K P, Samant M G, Rice P M, Beyers R B, Scheuerlein R E, O'Sullivan E J, Brown S L, Bucchigano J, Abraham D S, Lu Y, Rooks M, Trouilloud P L, Wanner R A and Gallagher W J 1999 *J. Appl. Phys.* **85** 5828
[12] Childress J R, Schwickert M M, Rontana R E, Ho M K, Rice P M and Gurney B A 2001 *J. Appl. Phys.* **89** 7353
Wang J U, Freitas P P, Snoeck E, Batlle X and Cuadra J 2002 *IEEE Trans. Magn.* **38** 2703
Araki S, Sato K, Kagami T, Saruki S, Uesugi T, Kasahara N, Kuwashima T, Ohta N, Sun J, Nagai K, Li S, Hachisuka N, Hatate H, Kagotani T, Takahashi N, Ueda K and Matsuzaki M 2002 *IEEE Trans. Magn.* **38** 72
[13] MacLaren J M, Zhang X-G, Butler W H and Wang X 1999 *Phys. Rev.* B **59** 5470
[14] Butler W H, Zhang X-G, Schulthess T C and MacLaren J M 2001 *Phys. Rev.* B **63** 054416
[15] Mathon J and Umerski A 2001 *Phys. Rev.* B **63** 220403(R)
[16] Wunnicke O, Papanikolaou N, Zeller R, Dederichs P H, Drchal V and Kudmovsky J 2002 *Phys. Rev.* B **65** 064425
[17] Freyss M, Papanikolaou N, Bellini V, Zeller R and Dederichs P H 2002 *Phys. Rev.* B **66** 014445
[18] Mavropoulos P, Wunnicke O and Dederichs P H 2002 *Phys. Rev.* B **66** 024416
[19] Landauer R 1957 *IBM J. Res. Dev.* **1** 223
[20] Büttiker M 1988 *IBM J. Res. Dev.* **32** 317
[21] Krstić P S, Zhang X-G and Butler W H 2002 *Phys. Rev.* B **66** 205319
[22] Meservey R and Tedrow P M 1994 *Phys. Rep.* **238** 174
[23] Monsma D J and Parkin S S P 2000 *J. Appl. Phys.* **77** 720
Monsma D J and Parkin S S P 2000 *J. Appl. Phys.* **77** 883
[24] MacLaren J M, Zhang X-G and Butler W H 1997 *Phys. Rev.* B **56** 11827
[25] Slonczewski J C 1989 *Phys. Rev.* **39** 6995
[26] Butler W H, Zhang X-G, Schulthess T C and MacLaren J M 2001 *Phys. Rev.* B **63** 092402
[27] MacLaren J M, Crampin S, Vvedensky D D and Pendry J B 1989 *Phys. Rev.* B **40** 12164
[28] Stiles M D and Hamann D R 1988 *Phys. Rev.* B **38** 2021
[29] Stiles M D and Hamann D R 1990 *Phys. Rev.* B **41** 5280
[30] Perdew J P and Zunger A 1981 *Phys. Rev.* **23** 5048
[31] Ceperley D M and Alder B J 1980 *Phys. Rev. Lett.* **45** 566
Ceperley D M 1978 *Phys. Rev.* B **18** 3126
[32] Vosko S H, Wilk K and Nusair M 1989 *Can. J. Phys.* **58** 1200
[33] Mavropoulos P, Papanikolaou N and Dederichs P H 2000 *Phys. Rev. Lett.* **85** 1088
[34] Oleinik I I, Tsymbal E Yu and Pettifor D G 2000 *Phys. Rev.* B **62** 3952
[35] Oleinik I I, Tsymbal E Yu and Pettifor D G 2002 *Phys. Rev.* B **65** 020401
[36] Butler W H, Zhang X-G, Wang X-D, van Ek J and MacLaren J M 1997 *J. Appl. Phys.* **81** 5518
[37] Li C and Freeman A J 1991 *Phys. Rev.* B **43** 780
[38] Schönberger U and Aryasetiawan F 1995 *Phys. Rev.* B **52** 8788
[39] Whited R C, Flaten C J and Walker W C 1973 *Solid State Commun.* **13** 1903
[40] Meyerheim H L, Popescu R, Kirschner J, Jedrecy N, Sauvage-Simkin M, Heinrich B and Pinchaux R 2001 *Phys. Rev. Lett.* **87** 076102
[41] Meyerheim H L, Popescu R, Jedrecy N, Sauvage-Simkin M, Pinchaux R, Heinrich B and Kirschner J 2002 *Phys. Rev.* B **65** 144433
[42] Zhang X-G and Butler W H 2003 *Phys. Rev.* B **68** 092402
[43] Faulkner J S and Stocks G M 1980 *Phys. Rev.* B **21** 3222
[44] Wachutka G and Bross H 1982 *J. Phys.* A **15** 3083
[45] Wachutka G 1986 *Phys. Rev.* B **34** 8512